

PUCRS

SCHOOL OF TECHNOLOGY  
GRADUATE PROGRAM IN ELECTRICAL ENGINEERING  
MASTER'S IN ELECTRICAL ENGINEERING

PHELIPI NUNES SCHUCK

**QUANTITATIVE ANALYSIS OF DYNAMIC AND STATIC [<sup>11</sup>C]-PK11195 PET IMAGES FOR  
MULTIPLE SCLEROSIS**

Porto Alegre  
2020

PÓS-GRADUAÇÃO - *STRICTO SENSU*



Pontifícia Universidade Católica  
do Rio Grande do Sul

**PHELIPI NUNES SCHUCK**

**QUANTITATIVE ANALYSIS OF DYNAMIC AND STATIC [<sup>11</sup>C]-PK11195 PET  
IMAGES FOR MULTIPLE SCLEROSIS**

Dissertation presented as a requirement for the Degree of Master in the Graduate Program in Electrical Engineering of the School of Technology at the Pontifical Catholic University of Rio Grande do Sul.

Concentration Area: Signals, Systems, and Information Technology.

Line of Research: Biomedical Engineering

Supervisor: Ana Maria Marques da Silva

Co-supervisor: Michel Koole

**Porto Alegre  
2020**

## Ficha Catalográfica

S384q Schuck, Phelipi Nunes

Quantitative Analysis of Dynamic and Static [11C]-PK11195 PET  
Images for Multiple Sclerosis / Phelipi Nunes Schuck . – 2020.

69 p.

Dissertação (Mestrado) – Programa de Pós-Graduação em  
Engenharia Elétrica, PUCRS.

Orientadora: Profa. Dra. Ana Maria Marques da Silva.

Co-orientador: Prof. Dr. Michel Koole.

1. PET. 2. Quantification. 3. Neuroinflammation. 4. PK11195. 5.  
Multiple Sclerosis. I. Marques da Silva, Ana Maria. II. Koole, Michel.  
III. Título.

**QUANTITATIVE ANALYSIS OF DYNAMIC AND STATIC  
[<sup>11</sup>C]-PK11195 PET IMAGES FOR MULTIPLE SCLEROSIS**

**CANDIDATE: PHELIPY NUNES SCHUCK**

This Master's Dissertation was judged to obtain the title of MASTER IN ELECTRICAL ENGINEERING and approved in its final form by the Graduate Program in Electrical Engineering at the Pontificia Universidade Católica do Rio Grande do Sul.

Aprovada em: 30 de Março de 2020



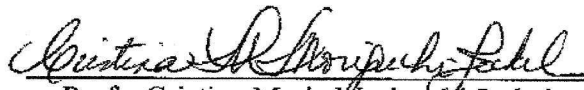
\_\_\_\_\_  
Prof. Dra. Ana Maria Marques da Silva  
Graduate Program in Electrical Engineering – PUCRS – Supervisor



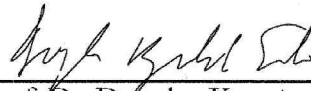
\_\_\_\_\_  
Prof. Dr. Michel Koole  
School of Medicine – KU Leuven/Belgium – Co-Supervisor

**EXAMINATION BOARD**

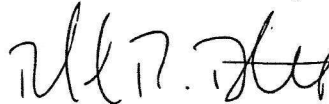
---



\_\_\_\_\_  
Prof. Cristina Maria Moriguchi Jeckel  
Graduate Program in Biomedical Gerontology – PUCRS



\_\_\_\_\_  
Prof. Dr. Douglas Kazutoshi Sato  
Graduate Program in Medicine and Healthy Sciences – PUCRS



\_\_\_\_\_  
Prof. Dr. Rafael Reimann Baptista  
Graduate Program in Electrical Engineering – PUCRS

**Porto Alegre  
2020**

*To everyone with autoimmune diseases,  
especially Multiple Sclerosis.*

## ACKNOWLEDGEMENTS

*Meus primeiros agradecimentos vão para os meus pais, Alexandre e Paula, que sempre me motivaram e me inspiraram a ser uma pessoa melhor, e que nunca deixaram de me apoiar nos momentos difíceis e que quando eu caí, estavam lá para me levantar.*

*Agradeço às minhas irmãs Melissa, Nicole e Sofia, que mesmo de longe e mesmo sem saber, foram importantes nessa caminhada. Espero que um dia eu possa ser um exemplo de irmão mais velho para vocês.*

*Gostaria de agradecer a minha orientadora, Professora Ana Maria, que me acompanha e orienta desde o início da minha carreira acadêmica. Obrigado por ser a minha mãe acadêmica, que sempre acreditou em mim e me apoiou em todos os momentos.*

I would like to thank my co-supervisor, Michel Koole. Thank you very much for having received me in your laboratory at Leuven, and for all the availability to support me.

*Agradeço a minha namorada, Adrielle, que esteve comigo em todos os momentos desse mestrado, e a sua família por todos momentos especiais. Obrigado por ter ido até o outro lado do oceano para matar a saudade durante meu intercâmbio.*

*Agradeço a minha amiga, companheira de pesquisa, laboratório e intercâmbio, Caroline. Obrigado pela companhia diária e principalmente por ter se jogado de cabeça comigo nessa jornada ao outro lado do oceano em busca de conhecimento.*

*Agradeço a professora Michele Alberton e a Dra. Cristina Matushita pelas grandes contribuições para este projeto e para o meu desenvolvimento pessoal e profissional, não só como colegas, mas também como amigas.*

*Agradeço aos amigos de fé, Nilson, Fellipe, Nícollas, Adriel, Nicolás, Thais, que sempre estiveram presentes em qualquer momento, fossem eles bons ou ruins*

*Por fim, agradeço aos demais familiares, colegas e professores que mesmo de longe sempre torceram pelo meu sucesso.*

This study was financed in part by the Coordenação de Aperfeiçoamento de Pessoal de Nível Superior – Brasil (CAPES) – Finance Code 001.

This work has been partially supported by the ENEN+ project from the Euratom research and training Work Programme 2016 – 2017 – 1 #755576

*A todos, muito obrigado.*

## ABSTRACT

PK11195 is a molecule with binding affinity with translocator protein (TSPO or 18-kDa), present in inflammatory activation. Imaging with positron emission tomography (PET) using [ $^{11}\text{C}$ ]-( $\text{R}$ )-PK11195 plays an important role in assessing the activated microglia in neuroinflammatory diseases. This study aimed to investigate different [ $^{11}\text{C}$ ]-( $\text{R}$ )-PK11195 PET quantification methods to estimate parameters that can be related to multiple sclerosis (MS) inflammation. The study used a longitudinal dataset consisting of PET and magnetic resonance (MR) images acquired from thirty-four human subjects along twenty-four months (ten healthy controls; twelve MS subjects with previous treatment; and twelve MS subjects without previous treatment). Different algorithms for segmenting brain regions were evaluated using T1 and T2-weighted MR images. Dynamic PET images were used to quantify the distribution volume ( $V_T$ ) and distribution volume ratio (DVR). Five models were tested using dynamic PET data: two tissue compartmental model (2TCM); Logan plot with  $t^* = 20$  min (LOG20); Logan plot with  $t^* = 40$  min (LOG40); reference Logan plot with  $t^* = 20$  min using normal-appearing grey matter (NAGM) as the reference region (rLOG20-NAGM); and reference Logan plot with  $t^* = 20$  min using normal-appearing whole-brain without ventricles (NAWB-V) as the reference region (rLOG20-NAWB-V). Static PET images were analyzed using two methods: standardized uptake value ratio (SUVR) using NAGM as the reference region, and SUVR using NAWB-V as the reference region. For MR images segmentation, the algorithm Lesion Segmentation Toolbox (LST) showed the lowest variability. The parameter DVR using the rLOG20-NAWB-V model showed the best differentiation between MS and healthy subjects, both in transversal and longitudinal studies, as well as the SUVR with the same reference region. The SUVR method using the normal-appearing whole-brain without ventricles as the reference region stands an excellent alternative to aid the MS diagnosis in clinical practice, due to the compatibility with the dynamic PET quantification.

**Keywords:** *PET; Quantification; Segmentation; Neuroinflammation; PK11195; Multiple Sclerosis.*

## RESUMO

*PK11195 é uma molécula com afinidade com a proteína translocadora (TSPO ou 18kDa), presente na ativação inflamatória. A tomografia por emissão de pósitrons (PET), usando [<sup>11</sup>C]-(R)-PK11195 tem um papel importante na avaliação da ativação microglial em doenças neuroinflamatórias. Esse estudo tem como objetivo investigar diferentes métodos de quantificação de PET com [<sup>11</sup>C]-(R)-PK11195 para estimar parâmetros que podem ser relacionado ao diagnóstico e evolução da esclerose múltipla (MS). O estudo utilizou um conjunto de dados longitudinal consistindo em PET e imagens por ressonância magnética (MR) adquiridas de 34 sujeitos ao longo de 24 meses (10 sujeitos saudáveis, 12 sujeitos com MS previamente tratados e 12 sujeitos com MS sem tratamento). Diferentes algoritmos de segmentação de regiões cerebrais foram avaliados utilizando imagens por MR ponderadas em T1 e T2. Imagens dinâmicas de PET foram utilizadas para quantificar o volume de distribuição ( $V_T$ ) e a razão do volume de distribuição (DVR). Cinco modelos foram avaliados usando imagens dinâmicas de PET: modelo compartimental de dois tecidos (2TCM); modelo gráfico de Logan com  $t^* = 20$  min (LOG20); modelo gráfico de Logan com  $t^* = 40$  min (LOG40); modelo gráfico de Logan com referência em  $t^* = 20$  min, utilizando a substância cinzenta aparentemente normal (NAGM) como região de referência (rLOG20-NAGM); e modelo gráfico de Logan com referência em  $t^* = 20$  min, utilizando o cérebro aparentemente normal sem os ventrículos (NAWB-V) como região de referência (rLOG20-NAWB-V). Imagens estáticas de PET foram analisadas usando dois métodos: razão do valor de captação padronizado (SUVR) utilizando a NAGM como região de referência, e SUVR utilizando a NAWB-V como região de referência. Para a segmentação das imagens por MR, o algoritmo Lesion Segmentation Toolbox (LST) mostrou menor variabilidade. O parâmetro DRV utilizando o modelo rLOG20-NAWB-V apresentou melhor diferenciação entre sujeitos com MS e saudáveis, tanto em análise transversal como em longitudinal, assim como SUVR, com a mesma região de referência. O método SUVR utilizando NAWB-V como referência representa uma excelente alternativa para auxiliar o diagnóstico de MS na prática clínica, devido à compatibilidade com a quantificação de imagens dinâmicas de PET.*

**Palavras chave:** PET; Quantificação; Segmentação; Neuroinflamação; PK11195; Esclerose Múltipla.



## LIST OF FIGURES

Figure 1. PET imaging scheme .....	20
Figure 2. 2TCM Graphical representation.....	24
Figure 3. SRTM Graphical representation. ....	25
Figure 4. LGM plot example. ....	26
Figure 5. Example of T1 weighted MRI (A) and T2-FLAIR MRI (B) acquired in this study. .....	33
Figure 6. Example of PET image with 23 time frames. ....	34
Figure 7. Example of static PET image.....	34

## LIST OF GRAPHS

Graph 1. Box plots of the volumes segmented from MRI obtained with all software.....	40
Graph 2. Box plots of WM volumes segmented for each software per group. In blue the WM volumes for MS subjects and yellow for HC. ....	41
Graph 3. Box plots of GM volumes segmented for each software per group. In blue the GM volumes for MS subjects and yellow for HC .....	41
Graph 4. Box plots of WB volumes segmented for each software per group. In blue the WM volumes for MS subjects and yellow for HC. ....	42
Graph 5. Box plot of $V_T$ determined from 2TCM per group (transversal analysis). In blue the MS subjects and green the healthy subjects. ....	43
Graph 6. Box plot of VT determined from the graphical Logan model ( $t^* = 20$ min) per group (transversal analysis). In blue the MS subjects and green the healthy subjects. ....	44
Graph 7. Box plot of VT determined from the graphical Logan model ( $t^* = 40$ min) per group (transversal analysis). In blue the MS subjects and green the healthy subjects. ....	45
Graph 8. Box plot of VT determined from the graphical Logan model ( $t^* = 20$ min) for MS naïve subjects in two time-points (baseline in blue and 6 months after fingolimod treatment in green).....	46
Graph 9. Box plot of VT determined from the graphical Logan model ( $t^* = 40$ min) for MS naïve subjects in two time-points (baseline in blue and 6 months after fingolimod treatment in green).....	46
Graph 10. Box plot of DVR determined from the reference Logan model ( $t^* = 20$ min) using NAGM as the reference, per group (transversal analysis).....	48
Graph 11. Box plot of DVR determined from the reference Logan model ( $t^* = 20$ min) using NAWB-V as the reference, per group (transversal analysis). In blue the MS subjects and green the healthy subjects.....	48
Graph 12. Box plot of DVR determined from the reference Logan model ( $t^* = 20$ min) using NAWB-V as the reference, in naïve MS subjects (longitudinal analysis). Blue is baseline, green is 6mo, beige is 12mo, and purple is 24mo. ....	49
Graph 13. Box plot of DVR determined from the reference Logan model ( $t^* = 20$ min) using NAWB-V as the reference, in pre-treated MS subjects (longitudinal analysis). Blue is baseline, green is 6mo, beige is 12 mo, and purple is 24mo. ....	50

Graph 14. Box plot of SUVR using NAGM as the reference, in MS subjects and HC (transversal analysis). In blue the MS subjects and green the healthy subjects. ....	51
Graph 15. Box plot of SUVR using NAGM as the reference, in naïve MS subjects (longitudinal analysis). In blue the MS subjects and green the healthy subjects. ....	52
Graph 16. Box plot of SUVR using NAWB-V as the reference, per group (transversal analysis). In blue the MS subjects and green the healthy subjects.....	52
Graph 17. Box plot of SUVR using NAWB-V as the reference, in naïve MS subjects (longitudinal analysis). In blue, the baseline, green 6mo, beige 12 mo, and purple 24mo. .	53
Graph 18. Box plot of SUVR using NAWB-V as the reference, in pre-treated MS subjects (longitudinal analysis). In blue, the baseline, green 6mo, beige 12 mo, and purple 24mo. .	53

## LIST OF TABLES

Table 1. Summary of the studies with [ <sup>11</sup> C]-(R)-PK11195 PET image quantification, applied to MS disease, in the last 5 years.....	29
Table 2. Demographic data of the study.....	31
Table 3. Mean and standard deviation of the volumes segmented with different software for each group.....	39

## LIST OF ABBREVIATIONS

11C	Carbon Eleven
18kDa	18 kilo Dalton
AIF	Arterial Input Function
beta+	beta plus particle
BPND	Binding Potential Non-Displaceable
BraIns	Brain Institute of Rio Grande do Sul
cm <sup>3</sup>	cubic centimeter
DMT	Disease Modification Therapy
DVR	Distribution Volume Ratio
EDSS	Expanded Disability Status Scale
FLAIR	Fluid Attenuation Inversion Recovery
FOV	Field of View
GE	General Electrics
GM	Gray Matter
IDIF	Image-Derived Input Function
kcps	kilo counts per second
LGM	Logan Graphical Model
LRM	Logan Reference Model
min	minute
mL	milliliter
mm	millimeter
MRI	Magnetic Resonance Imaging
MS	Multiple Sclerosis
ms	milliseconds

MSFC	Multiple Sclerosis Functional Composite
NAGM	Normal Appearing Gray Matter
NAWM	Normal Appearing White Matter
PET	Positron Emission Tomography
PK11195	(R)-PK11195(1-(2-chlorophenyl)-N-methyl-N-(1-methyl propyl)-3-isoquinoline carboxamide)
PUCRS	Pontificia Universidade Católica do Rio Grande do Sul
QSM	Quantitative Susceptibility Map
RRMS	Relapsing-Remitting Multiple Sclerosis
s	second
SRTM	Simplified Reference Tissue Modelling
SUV	Standardized Uptake Value
SUVR	Standardized Uptake Value Ratio
SVCA	Supervised Clustering Analysis
TSPO	Translocator Protein
VOI	Volume of Interest
VT	Total Distribution Volume
WM	White Matter

## TABLE OF CONTENTS

<b>1</b>	<b>INTRODUCTION</b> .....	<b>17</b>
<b>2</b>	<b>OBJECTIVES</b> .....	<b>18</b>
	2.1 GENERAL OBJECTIVE.....	18
	2.2 SPECIFIC OBJECTIVES .....	18
<b>3</b>	<b>BACKGROUND</b> .....	<b>19</b>
	3.1 POSITRON EMISSION TOMOGRAPHY .....	19
	3.2 MULTIPLE SCLEROSIS AND IMAGING .....	20
	3.3 PET QUANTIFICATION.....	22
	3.3.1 Quantitative Methods .....	22
	3.3.1.1 Compartmental models.....	22
	3.3.1.1.1 Two-tissue Compartment Model (2TCM).....	23
	3.3.1.1.2 Simplified Reference Tissue Model (SRTM).....	24
	3.3.1.2 Non-compartmental models.....	25
	3.3.1.2.1 Logan Graphical Model (LGM) .....	25
	3.3.1.2.2 Logan Reference Model (LRM) .....	26
	3.3.2 Semi-quantitative Methods .....	27
	3.4 STATE OF THE ART.....	27
<b>4</b>	<b>METHODS &amp; MATERIALS</b> .....	<b>31</b>
	4.1 CLINICAL STUDY .....	31
	4.2 PROCEDURES .....	31
	4.3 IMAGE ACQUISITION .....	32
	4.3.1 MRI Acquisition.....	32
	4.3.2 PET/CT Acquisition.....	33
	4.3.3 Image Processing and Analysis.....	35

4.3.3.1	MRI Processing .....	35
4.3.3.1.1	SPM8 .....	35
4.3.3.1.2	LST .....	35
4.3.3.1.3	FreeSurfer .....	36
4.3.3.1.4	SienaX.....	36
4.3.3.1.5	Juxtacortical and Periventricular Segmentation .....	37
4.3.3.2	PET Image Processing.....	37
4.3.4	Statistical Analysis .....	38
4.4	MRI SEGMENTATION ANALYSIS .....	38
4.5	PET ANALYSIS.....	38
<b>5</b>	<b>RESULTS.....</b>	<b>39</b>
5.1	MRI SEGMENTATION.....	39
5.2	DYNAMIC PET QUANTIFICATION.....	42
5.2.1	Image Derived Input Function .....	43
5.2.1.1	2TCM – Transversal Analysis .....	43
5.2.1.2	Graphical Logan Model – Transversal Analysis .....	44
5.2.1.2.1	Logan (t*=20min) – Transversal Analysis .....	44
5.2.1.2.2	Logan (t*=40min) – Transversal Analysis .....	44
5.2.1.3	Logan Graphical Model – Longitudinal Analysis .....	45
5.2.1.3.1	Logan (t*=20min).....	45
5.2.1.3.2	Logan (t*=40min).....	46
5.2.2	reference tissue modelling.....	47
5.2.2.1	Reference Logan with NAGM as reference (t*=20min) - Transversal Analysis .....	47
5.2.2.2	Reference Logan with NAWB-V as the reference (t*=20min) - Transversal Analysis .....	48
5.2.2.3	Reference Logan with NAWB-V as the reference (t*=20min) - Longitudinal Analysis .....	49



5.3	STATIC PET SEMI-QUANTIFICATION.....	50
5.3.1	SUVR with NAGM as reference.....	51
5.3.1.1	Transversal Analysis.....	51
5.3.1.2	Longitudinal Analysis.....	51
5.3.2	SUVR with NAWB-V as reference .....	52
5.3.2.1	Transversal Analysis.....	52
5.3.2.2	Longitudinal Analysis.....	53
<b>6</b>	<b>DISCUSSION.....</b>	<b>55</b>
6.1	MRI SEGMENTATION .....	55
6.2	DYNAMIC PET QUANTIFICATION.....	56
6.3	STATIC PET SEMI-QUANTIFICATION.....	58
<b>7</b>	<b>FINAL CONSIDERATIONS .....</b>	<b>60</b>
<b>8</b>	<b>REFERENCES .....</b>	<b>61</b>

# 1 INTRODUCTION

Positron emission tomography (PET) allows the assessment of physiology or function through molecules labelled with radioisotopes, called radiotracers (CHERRY; SORENSON; PHELPS, 2012). PET is the imaging technique of choice for cancer tracking and neurological disease diagnosis.

The molecule PK11195 labelled with  $^{11}\text{C}$  ( $[^{11}\text{C}]$ -(R)-PK11195) binds with activated microglia in neuroinflammation and can be visualized in both static and dynamic PET imaging. Some authors quantify the relative uptake between a region of interest and a reference region in static  $[^{11}\text{C}]$ -(R)-PK11195 PET images (HAMMOUD et al., 2005; KAUNZNER et al., 2017, 2019; RISSANEN et al., 2018). An alternative approach, called absolute quantification or kinetic modelling, requires a dynamic PET acquisition, allowing the assessment of physiological and biochemical parameters, through compartment models and arterial blood sampling (INNIS et al., 2007; KANG et al., 2018b; KOBAYASHI et al., 2018; RIZZO et al., 2017; ZANOTTI-FREGONARA et al., 2011). Another approach, less invasive than the previous one, is the use of simplified reference tissue models, without blood sampling (KROPHOLLER et al., 2007, 2005; LAMMERTSMA; HUME, 1996; PARBO et al., 2018; PASSAMONTI et al., 2018; RIZZO et al., 2017). In the last 12 years, several  $[^{11}\text{C}]$ -(R)-PK11195 PET quantification methods have been investigated for different inflammatory diseases.

This work aimed to investigate different  $[^{11}\text{C}]$ -PK11195 PET quantification methods for multiple sclerosis (MS) neuroinflammation, evaluating the challenges and pitfalls of each method.

## **2 OBJECTIVES**

### **2.1 GENERAL OBJECTIVE**

This study aimed to investigate different [ $^{11}\text{C}$ ]-( $\text{R}$ )-PK11195 PET quantification methods to estimate parameters that can be related to multiple sclerosis (MS) neuroinflammation.

### **2.2 SPECIFIC OBJECTIVES**

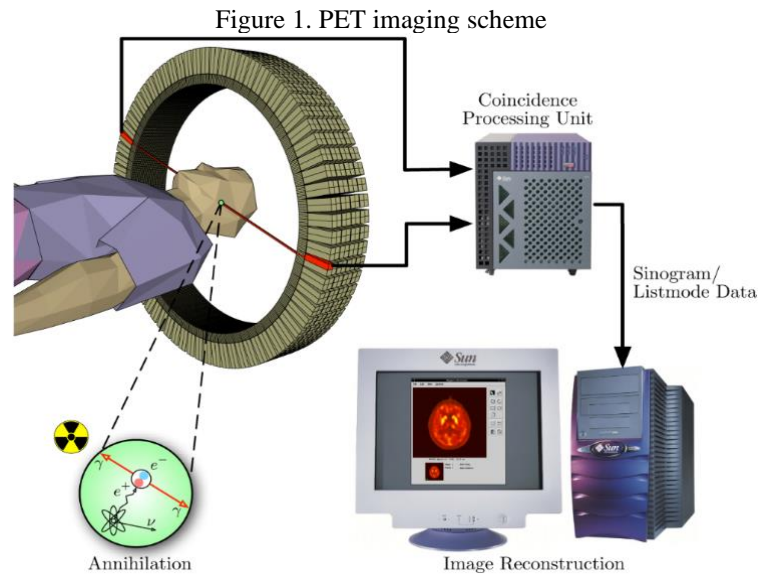
- To investigate different magnetic resonance imaging segmentation algorithms to extract brain structures relevant to the MS analysis.
- To investigate different [ $^{11}\text{C}$ ]-( $\text{R}$ )-PK11195 PET quantification methods to estimate parameters from dynamic PET data.
- To investigate different [ $^{11}\text{C}$ ]-( $\text{R}$ )-PK11195 PET semi-quantification methods to estimate parameters from static PET data.

## 3 BACKGROUND

### 3.1 POSITRON EMISSION TOMOGRAPHY

Positron Emission Tomography (PET) is a nuclear imaging technique that uses molecules labelled with isotopes (radiotracer) used to acquire functional images. The most important characteristics of PET are its quantitative nature and its extremely high sensitivity, allowing measurements down to picomolar level (CHERRY; SORENSON; PHELPS, 2012).

In PET imaging the radionuclide emits  $\beta^+$  particles, also called positrons. The positron, when emitted by the unstable nucleus, loses its kinetic energy due to the collisions in the atoms of the nearby tissues. A few millimeters after emission, it interacts with an electron of the medium forming the positronium, with approximately 0.1 ps half-life. The annihilation begins when the positron and the electron interact, transforming their masses into energy in the form of two annihilation photons (CHERRY; SORENSON; PHELPS, 2012; ROBILOTTA, 2006). In electron-positron pair annihilation, photons energy is usually 0.511 MeV, due to the mass-energy equivalence, almost emitted at  $180^\circ$  (EISBERG; RESNICK, 1979). PET acquisition consists of coincidence detection of annihilation photons by detectors positioned in a circular ring around the field of view (FOV), where the radionuclide site is located. The system detects the simultaneous interactions, called coincidence event, in two detectors along the line connecting the detectors in opposite directions. Each pair of parallel and opposite detectors produces a coincidence line. PET image is recorded when a coincidence event is within the coincidence window interval, usually 6 to 12 ns, generating a line of response (CHERRY; SORENSON; PHELPS, 2012). If a coincidence line is recorded, PET image can be mathematically reconstructed from the raw data (sinogram) collected in all directions during the scanning. Figure 1 shows a representation of the PET imaging process, showing the subject inside the ring of detectors, and a pair of annihilation photons being detected and producing a line of response, recorded in the coincidence processing unit. The coincidence events are stored in the sinogram, in which one direction represents the offset from the center of the field of view, whereas the other direction describes the projection angle. The sinogram provides a set of projection data for the image reconstruction using mathematical algorithms.



Source: (LANGNER, 2003).

### 3.2 MULTIPLE SCLEROSIS AND IMAGING

Multiple sclerosis (MS) is an autoimmune disease of the central nervous system characterized by inflammation, demyelination, and gradual neuronal loss. It has a high social impact because it is usually diagnosed in young adults, between 18 and 40 years. (FINKELSZTEJN, 2009; GIANNETTI *et al.*, 2014a; THOMPSON *et al.*, 2018). MS has two main clinical phenotypes, one with a slow but progressive increase in disability and another with acute exacerbations known as relapses (relapsing-remitting form). The latter being the most common initial disease form: 70–93% (NEGROTTO; CORREALE, 2018). Relapsing-remitting multiple sclerosis (RRMS) subjects have clinical stability between relapses, which worsen over time, and may or may not produce persistent neurological sequela. In progressive MS subjects, the disease progressively advances with or without relapses (FINKELSZTEJN, 2009; THOMPSON *et al.*, 2018).

MS diagnosis is made based on the clinical features, supported by typical lesions on the MRI. In some cases, cerebrospinal fluid may reveal the presence of immunoglobulin G oligoclonal bands (OCB) exclusively produced intrathecally. When subjects are diagnosed, they are classified using the expanded disability status scale (EDSS). Scores are calculated according to their functional scores, such as visual, motor, sensory, and other functions. The EDSS scale has a range from 0 to 10, wherein EDSS = 0 the patient does not present any neurological sign, and EDSS = 10 the patient goes to death due to the disease (FINKELSZTEJN, 2009; KURTZKE, 1983; THOMPSON *et al.*, 2018).

Currently, the MS diagnostic criteria are based on the revised McDonald Criteria 2017 (THOMPSON *et al.*, 2018), which includes the presence of clinical relapses, typical demyelinating lesions, OCB in the CSF, and progressive accrual of disability for progressive forms. The lesions dissemination can be verified with their presence in at least two of the four characteristics regions: juxta cortical, periventricular, infratentorial, and spinal cord (THOMPSON *et al.*, 2018). Meanwhile, the dissemination in time can be verified with the presence of active T1-Gd+ and T2WI lesions on a single MRI or new lesions, in comparison to previous MRI (THOMPSON *et al.*, 2018).

T1 hypointense (black holes) lesions in MS represent axonal loss and can be visualized on T2-weighted MRI using the FLAIR sequence, with or without gadolinium contrast (GIANNETTI *et al.*, 2014; THOMPSON *et al.*, 2018). All MS lesions present high intensity in T2-weighted MR; however, black holes present low signal images on T1-weighted MRI after or during neuroinflammation (GIANNETTI *et al.*, 2014a; SCHMIDT *et al.*, 2012).

(R)-PK11195(1-(2-chlorophenyl)-N-methyl-N-(1-methylpropyl)-3-isoquinolinecarboxamide) enantiomer, when labelled with  $^{11}\text{C}$  is a neuroinflammatory marker that can be visualized in PET (VOWINCKEL *et al.*, 1997). This is due to the affinity between PK11195 and translocating protein (18 kDa) or TSPO, which is present in the central nervous system at low levels when the subject is healthy, and increases when there is activated neuroinflammation (BANATI, 2002; CASELLAS; GALIEGUE; BASILE, 2002; CHAUVEAU *et al.*, 2008; SCHWEITZER *et al.*, 2010). Its major use is in neurodegenerative diseases diagnoses, such as Alzheimer's disease (ANDERSON *et al.*, 2007; GROOM *et al.*, 1995; KROPHOLLER *et al.*, 2007; TOMASI *et al.*, 2008) and MS (BANATI, 2002; DEBRUYNE *et al.*, 2002; VERSIJPT *et al.*, 2005).

Other generations of TSPO tracers were developed to increase the power of inflammation detection. Nevertheless, the use [ $^{11}\text{C}$ ]-PBR28 and [ $^{18}\text{F}$ ]-GE-180 in clinical trials is a great challenge, due to the polymorphism detected in Caucasian people (OWEN *et al.*, 2012; VOMACKA *et al.*, 2017), generating bias in the binding affinity.

In PET images acquired with [ $^{11}\text{C}$ ]-PK11195, MS lesions usually appear with low uptake when not active and high uptake if still active (GIANNETTI *et al.*, 2014).

Inflammatory activities caused by MS generate the activation of microglia, intrinsic macrophage of the brain, producing neuronal damage. Studies report the increases of TSPO

binding density with microglia activation since TSPO is expressed outside of the mitochondrial membrane, in the activated microglia (SCHWEITZER et al., 2010). The abundant concentration of 18 kDa becomes a potential PET biomarker; the macrophages accumulation is a suitable target for [<sup>11</sup>C]-(R)-PK11195 quantification (HINZ; BOELLAARD, 2015; SCHWEITZER et al., 2010).

[<sup>11</sup>C]-(R)-PK11195 allows the quantification and visualization of activated microglia (BANATI, 2002), using dynamic or static PET/CT images (LAMMERTSMA; HUME, 1996). However, the discussion about [<sup>11</sup>C]-(R)-PK11195 PET quantification methods to aid MS diagnosis and evolution of the disease still has problems and it is not standardized.

### **3.3 PET QUANTIFICATION**

PET offers a high potential for quantitative characterization of in vivo molecular processes (BUVAT, 2007). PET quantification can be done by kinetic modelling, which allows absolute quantification through values extracted from time-activity curves (TAC) in dynamic images (CARSON, 2003); and semi-quantification, so-called because it is not done with real activity concentration values, but with averages over time, in static PET images (DEBRUYNE *et al.*, 2002).

#### **3.3.1 QUANTITATIVE METHODS**

PET absolute quantification or kinetic modelling allows the assessment of physiological or biochemical parameters, such as Distribution Volume ( $V_T$ ), Binding Potential (BP), and Distribution Volume Ratio (DVR) through compartment models (INNIS *et al.*, 2007). These parameters can be evaluated through different methods, such as compartmental and non-compartmental models, described in the next sections.

##### **3.3.1.1 Compartmental models**

The knowledge of the biochemical and physiological behavior of a radiotracer in tissue is the basis for developing a mathematical compartmental model to describe the observed data. Compartments are commonly used in the pharmacokinetics field to define physiologically separate pools of tracer substances, whether in space or time.

In PET imaging compartmental models are evaluated through two approaches. The first is the acquisition of the arterial input function (AIF). It is considered the kinetic modelling gold standard, nevertheless highly invasive and demanding, requiring arterial blood sampling during all image acquisition. The second approach uses reference tissue models that replace AIF by an indirect input function extracted from image data, not requiring blood sampling (KROPHOLLER *et al.*, 2007, 2005; LAMMERTSMA; HUME, 1996).

Recent studies in [<sup>11</sup>C]-(*R*)-PK11195 PET quantification are using two-tissue compartment model (2TCM), where AIF is extracted from blood sampling (JUČAITE *et al.*, 2012; KOBAYASHI *et al.*, 2018; RIZZO *et al.*, 2017). Other approach uses the simplified reference tissue model (SRTM), where regions/tissues are used as input function (KROPHOLLER *et al.*, 2006; LAMMERTSMA; HUME, 1996; PASSAMONTI *et al.*, 2018; RIZZO *et al.*, 2017; STOKHOLM *et al.*, 2017). Finally, other current approach extract the image-derived input function (IDIF) through the segmentation of arteries in other imaging modalities, such as MRI and CT, avoiding arterial sampling (CROTEAU *et al.*, 2010; KANG *et al.*, 2018a; KAUNZNER *et al.*, 2019; POLITIS *et al.*, 2012).

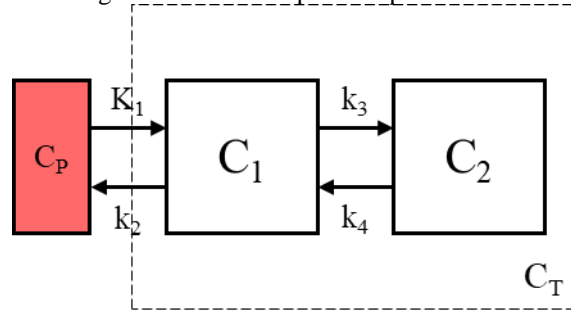
More details about two compartmental models used in this work are given in the next sub-sections: (1) two-tissue compartment model (2TCM); (2) simplified reference tissue model (SRTM).

#### 3.3.1.1.1 Two-tissue Compartment Model (2TCM)

The tracer concentration in the tissue is affected by tracer flow from the blood into the tissue and by the tracer loss from the tissue. The 2TCM represents the tissue or region of interest as two compartments ( $C_1$  and  $C_2$ ). Arterial plasma ( $C_p$ ) exchanges tracer with the compartment  $C_1$  with an uptake rate  $K_1$  [mL/cm<sup>3</sup>/min] and clearance rate  $k_2$  [1/min], where there is free and non-specifically bound tracer in the tissue (non-displaceable compartment). The compartment  $C_2$ , called the bound tracer compartment, exchanges tracer with  $C_1$  with exchanging rates  $k_3$  [1/min] and  $k_4$  [1/min]. The total amount of tracer on the tissue is represented as  $C_T$ . Figure 2 shows a graphical representation of the 2TCM.



Figure 2. 2TCM Graphical representation



Source: The Author, (2020)

The differential equations 1 and 2 estimate the kinetic modelling between the compartments in 2TCM. Equation 1 describes the exchange rate of free and non-specifically bound tracer in  $C_1$  with the plasma and  $C_2$  compartments, while equation 2 describes the exchange rate in  $C_2$  of specifically bound tracer with the compartment  $C_1$ :

$$\frac{dC_1(t)}{dt} = K_1 C_P(t) - (k_2 + k_3) C_1(t) + k_4 C_2(t) \quad (1)$$

$$\frac{dC_2(t)}{dt} = k_3 C_1(t) - k_4 C_2(t) \quad (2)$$

### 3.3.1.1.2 Simplified Reference Tissue Model (SRTM)

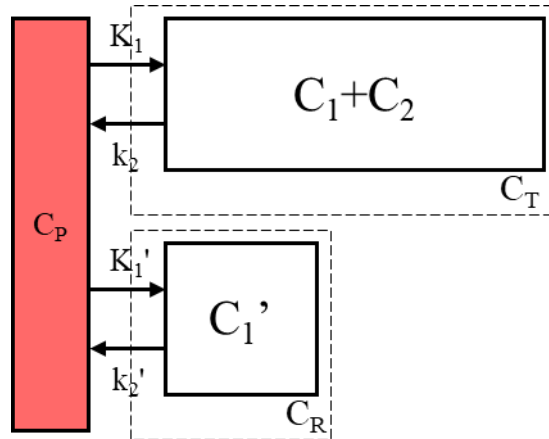
This model is used to analyze radiotracers with reversibly binding receptors. In SRTM, a reference tissue without receptors is required for SRTM calculation (LAMMERTSMA; HUME, 1996); however, studies indicate that pseudo-reference tissues can also be used (ALBRECHT *et al.*, 2018; LYOO *et al.*, 2015). The assumption of SRTM is the ratio ( $R_1$ ) between the exchange constant rates between  $C_P$  and  $C_1$ , and  $C_P$  and  $C_1'$  (reference tissue), are equivalent. This assumption is represented in equation 3:

$$R_1 = \frac{K_1}{k_2} = \frac{K_1'}{k_2'} \quad (3)$$

where  $K_1'$  represents the uptake rate [mL/cm<sup>3</sup>/min] and  $k_2'$  [1/min] the clearance, both in the reference tissue.

Figure 3 shows SRTM representation, where  $C_1$  represents the free and non-specifically bound tracer in the tissue,  $C_2$  is the specifically bound tracer compartment,  $C_T$  is the amount of tracer in the tissue of interest,  $C_1'$  and  $C_R$  are the tracer amount in the reference tissue, and  $K_1, k_2, K_1'$  and  $k_2'$  represent the exchange constant rates.

Figure 3. SRTM Graphical representation.



Source: The Author (2020)

Differential equation 4 estimates the kinetic modelling calculation:

$$\frac{dC_1(t)}{dt} = R_1 \frac{dC_1'(t)}{dt} + k_4 C_1'(t) - \frac{k_2}{1 + BP_{ND}} C_1(t) \quad (4)$$

where  $BP_{ND}$  is the non-displacement binding potential, calculated through  $k_3/k_4$  ratio.

### 3.3.1.2 Non-compartmental models

In non-compartment models, the input function and time-activity curves (TACs) of volumes of interest (VOIs) are transformed and combined into a single curve, that approaches linearity when certain conditions are reached. The data are plotted in a graph, and a straight line can be fitted to the linear phase. This calculation can be performed through Logan graphical model (LOGAN *et al.*, 1990), that was developed for reversible tracers, which means tracer can flow in both ways, inside and outside the tissue, such as  $[^{11}\text{C}]\text{-PK11195}$ . The graphical Patlak model is used to estimate kinetic parameters of irreversible tracers, where tracer only flows inside the tissue, (PATLAK; BLASBERG; FENSTERMACHER, 1983).

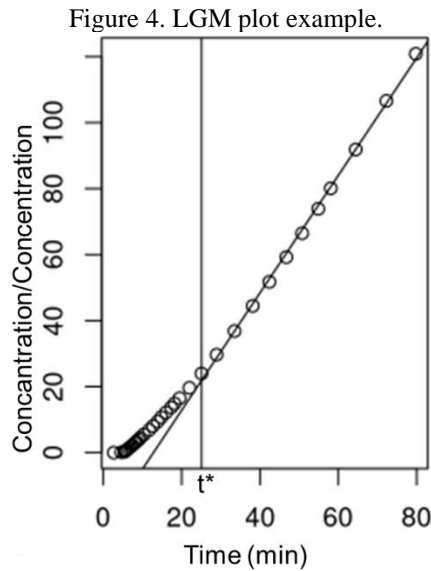
#### 3.3.1.2.1 Logan Graphical Model (LGM)

Logan plot is the most known graphical quantification method for reversible radiopharmaceuticals, used as an alternative for total distribution volume ( $V_T$ ) estimation. The measured tissue tracer concentration  $C_T(t)$  and the input function  $C_P(t)$  TAC is submitted to the mathematical transformation shown in equation (5).

$$\frac{\int_0^t C_T(\tau) d\tau}{C_T(t)} = V_T \frac{\int_0^t C_P(\tau) d\tau}{C_T(t)} + b \quad (5)$$

where  $V_T$  is the angular coefficient in the equation, and  $b$  is the linear coefficient of the linear equation.

Equation 5 means  $C_T(t)$  integrated from the time of injection is divided by the instantaneous tissue activity and plotted at a "normalized time" (integral of  $C_P(t)$  from the injection time divided by the instantaneous  $C_T(t)$ ). For systems with reversible compartments, this plot will result in a straight line after the equilibration time  $t^*$ . Figure 4 shows a LGM plot representation, where time  $t^*$  is indicated as the time-point where the ratio between the concentrations starts following a linear tendency.



Source: The Author (2020).

### 3.3.1.2.2 Logan Reference Model (LRM)

Logan reference model was developed as a substitute to the Logan graphical model, which does not require an arterial input function (AIF), replaced by a reference tissue acquired from the PET image. The reference tissue or region is usually assigned as a region without tracer specific binding or in clinical studies, regions with the same kinetic behavior in diseased and healthy subjects (LYOO *et al.*, 2015).

LRM allows the estimation of the distribution volume ratio (DVR), which also is the angular coefficient in the linearization equation. As in the LGM, LRM needs an equilibration time  $t^*$  to estimate the kinetic parameters in the linear equation, shown in equation 6.

$$\frac{\int_0^t C_T(\tau) d\tau}{C_T(t)} = DVR \left[ \frac{\int_0^t C_R(\tau) d\tau + \frac{C_R(t)}{k_2'}}{C_T(t)} \right] + b \quad (6)$$

where  $C_R(\tau)$  is the reference tissue concentration and  $k_2'$  is a constant rate used to estimate the tracer flow between tissues.

### 3.3.2 SEMI-QUANTITATIVE METHODS

When static PET images are used, only semi-quantitative parameters can be calculated (YODER, 2013). The most common semi-quantitative measurement is the standardized uptake value (SUV), which corresponds to the activity concentration (Bq/mL) in the region of interest (ROI) divided by the injected activity concentration by body mass (Bq/kg). SUV is valid only assuming the radioactive material is distributed throughout the whole body, in equilibrium (YODER, 2013). Equation 1 shows SUV calculation.

$$SUV = \frac{C_{ROI}}{A_{inj}/m_{subject}} \quad (7)$$

where  $C_{ROI}$  is the activity concentration in the ROI under analysis, and  $A_{inj}$  is the activity injected in the subject mass  $m_{subject}$ . SUV can be measured using the maximum or mean value in the region of interest (YODER, 2013).

Another semi-quantification method is the SUV ratio, termed SUVR, which is the ratio between SUV in the tissue of interest and a reference tissue (LOPRESTI *et al.*, 2005). Equation 2 shows SUVR calculation.

$$SUVR^{REF} = \frac{SUV_{ROI}}{SUV_{REF}} = \frac{\frac{C_{ROI}}{A_{inj}}}{\frac{C_{REF}}{A_{inj}}} = \frac{C_{ROI}}{C_{REF}} \quad (8)$$

where  $C_{REF}$  is the activity concentration in the reference region. SUVR is independent of the injected activity and it is calculated only using the ratio between activity concentrations.

## 3.4 STATE OF THE ART

Several studies using PET images with [ $^{11}\text{C}$ ]-(*R*)-PK11195 in MS studies have been performed since the '90s (VOWINCKEL *et al.*, 1997). The gold standard for PET quantification is through the activity measurement obtained from arterial input function, but

this is an invasive procedure, produces patient discomfort and increases the research costs (ZANOTTI-FREGONARA *et al.*, 2011). [<sup>11</sup>C]-(R)-PK11195 has a low specific binding and a high non-specific binding, which increases the difficulty to reach a standardization in quantification methods (CHAUVEAU *et al.*, 2008; SCHWEITZER *et al.*, 2010).

Our review showed that most papers about PET quantification with [<sup>11</sup>C]-(R)-PK11195 in MS are transversal studies (GIANNETTI *et al.*, 2014b; KANG *et al.*, 2018b; KAUNZNER *et al.*, 2019; RISSANEN *et al.*, 2018). Three studies with short term longitudinal analysis (6 months) were published after starting treatment with natalizumab (KAUNZNER *et al.*, 2017), fingolimod (SUCKSDORFF *et al.*, 2017) and glatiramer (RATCHFORD *et al.*, 2012). There is a lack of studies showing how to evaluate MS treatment during an extended period.

Most of [<sup>11</sup>C]-(R)-PK11195 studies use IDIF extracted from carotid arteries, manually delineated in the static PET imaging overlapped with MRI. They estimate  $V_T$  or  $V_T$  ratio between ROI and reference region, such as NAWM (KAUNZNER *et al.*, 2019) or reference region derived from supervised clustering analysis (SVCA) (KANG *et al.*, 2018a; KAUNZNER *et al.*, 2017; SUCKSDORFF *et al.*, 2017). Some studies use only reference tissue modelling and calculate DVR (RISSANEN *et al.*, 2014, 2018; SUCKSDORFF *et al.*, 2017) or  $BP_{ND}$  (GIANNETTI *et al.*, 2014b; KANG *et al.*, 2018b).

The discussion about [<sup>11</sup>C]-(R)-PK11195 PET quantification methods to investigate neuroinflammation in MS still has issues and a lack of standardization. Moreover, in the last 5 years (Table 1), publications about [<sup>11</sup>C]-(R)-PK11195 PET quantification emerged, and the scientific community is getting close to define a standard for [<sup>11</sup>C]-(R)-PK11195 PET processing and quantification. A standardized approach could contribute to the comprehension of MS disease and how the neuroinflammation spreads around the brain.

<b>Table 1. Summary of the studies with [<sup>11</sup>C]-(R)-PK11195 PET image quantification, applied to MS disease, in the last 5 years.</b>							
<b>Authors</b>	<b>(KAUNZNER et al., 2019)</b>	<b>(KANG et al., 2018a)</b>	<b>(RISSANEN et al., 2018)</b>	<b>(KAUNZNER et al., 2017)</b>	<b>(SUCKSDORFF et al., 2017)</b>	<b>(RISSANEN et al., 2014)</b>	<b>(GIANNETTI et al., 2014)</b>
<b>Objectives</b>	Provide imaging and histological evidence that QSM can identify chronic active multiple sclerosis lesions	Determine which PK modelling method provide the most robust and accurate measure of microglial activation	Evaluate whether microglial activation in the NAWM, measured cross-sectionally using in vivo PET	Use PK11195-PET to evaluate the PK11195 longitudinal uptake of MS subjects with natalizumab treatment	Determine the kinetics of microglial activation in various brain areas of a cohort of RRMS subjects	Evaluate whether TSPO imaging could be used to visualize the diffuse inflammation in WM	Examine PK binding in MS BHs as an indicator of microglial activity
<b>Subjects</b>	30 MS Subjects	10 MS Subjects	20 MS Subjects 8 Controls	24 MS Subjects 5 Controls	17 MS Subjects 8 Controls	10 MS Subjects 8 Controls	19 MS Subjects
<b>Software</b>	FreeSurfer PMOD	FreeSurfer PMOD SuperPK	SPM8 SuperPK Freesurfer	Freesurfer PMOD SuperPK	SPM8 LST SuperPK	SPM8 LST SuperPK	SPM2 SuperPK
<b>Regions of interest</b>	Lesions NAWM QSM	Cortical GM WM Thalamus	NAWM Thalamus Striatum Neocortex Cerebellum	NAWM Cortical GM Thalamus Lesion	Cortical Regions periventricular NAWM	Cortical Regions periventricular NAWM	Lesions
<b>Reference</b>	IDIF NAWM	IDIF SVCA 4	SVCA 4	IDIF SVCA	SVCA	SVCA	SVCA
<b>Kinetic Model Parameters</b>	$V_T$ $V_{Tr}(NAWM)$	$V_T$ BPND	DVR	$V_T$ $V_{Tr}$	DVR	DVR	BPND
<b>Quantification Method</b>	Logan Plot	Logan Plot Logan Reference	Logan Reference 20-60min	Logan Plot Logan Reference	Logan Reference 20-60min	Logan Reference	SRTM
<b>QSM – Quantitative susceptibility map; WM – White matter; NAWM – Normal Appearing White Matter; GM – Gray Matter; SVCA – Supervised Clustering Analysis.</b>							
<b>Source: The Author (2020)</b>							

The main challenge to [<sup>11</sup>C]-(R)-PK11195 PET quantification standardization is the lack of a reference region. No studies were found comparing kinetic parameters from models with AIF, IDIF or reference tissues between MS and healthy subjects to validate a reference region. Recent studies use mostly reference regions derived from supervised clustering analysis (SVCA) with SuperPK (GIANNETTI *et al.*, 2014; KANG *et al.*, 2018a; KAUNZNER *et al.*, 2017, 2019; POLITIS *et al.*, 2012; RATCHFORD *et al.*, 2012; RISSANEN *et al.*, 2014, 2018; SUCKSDORFF *et al.*, 2017). However, SuperPK is highly dependent on PET scanner characteristics (detectors, attenuation correction, motion correction, injection time) affecting the result of reference region estimative directly.

Beyond [<sup>11</sup>C]-(R)-PK11195 PET imaging, authors are including MRI data to increase the reliability of their results, such as MRI segmentation (GIANNETTI *et al.*, 2014; KANG *et al.*, 2018a; KAUNZNER *et al.*, 2017, 2019; POLITIS *et al.*, 2012; RATCHFORD *et al.*, 2012; RISSANEN *et al.*, 2014, 2018; SUCKSDORFF *et al.*, 2017). No consensus are found about MRI segmentation methods and which software must be used. Previous studies have been using Freesurfer (<https://surfer.nmr.mgh.harvard.edu/>), SPM (<https://www.fil.ion.ucl.ac.uk/spm/>), and PMOD (<https://www.pmod.com/web/>) for MRI segmentation, which could also provide differences in result.

This work aims to investigate [<sup>11</sup>C]-(R)-PK11195 PET images fully quantitative and semi-quantitative methods in multiple sclerosis neuroinflammation both in transversal and longitudinal studies.

## 4 METHODS & MATERIALS

### 4.1 CLINICAL STUDY

This study was performed with a database acquired by a clinical study at Brain Institute of Rio Grande do Sul (BraIns), PUCRS, Brazil. The study protocol was approved by PUCRS Ethics Committee (CAAE: 23949813.7.0000.5336). All participants signed a written informed consent form according to the Declaration of Helsinki.

Two groups of subjects with relapsing-remitting multiple sclerosis (RRMS) diagnosed according to the 2010 revised McDonald criteria (POLMAN *et al.*, 2011), which also fulfills 2017 revised McDonald criteria (THOMPSON *et al.*, 2018), were recruited. Twelve subjects with previous disease-modifying therapies (DMT) underwent to [<sup>11</sup>C]-PK11195 PET/CT and MRI, at 4 time-points (baseline, 6 months, 12 months, and 24 months). This group, designated PT, continued with previous DMT until the second time point and then started treatment with oral fingolimod daily. Twelve subjects without previous DMT, called naïve MS group designated N, also underwent the imaging protocol (PET/CT and MRI) at 4 time-points, differently, after the baseline they started treatment with oral fingolimod. All included patients had no relapses before at least 1 month before imaging. Thirteen healthy subjects, designated HC, were selected and underwent the same medical tests and imaging to be compared with subjects as a control group.

### 4.2 PROCEDURES

The pre-treated group (PT) was on average of ( $28 \pm 8$ ) years old. The naïve group (N) was on average of ( $30 \pm 8$ ) years old. The healthy-control group (HC) was ( $30 \pm 8$ ) years old. At each time point the Expanded Disability Status Scale (EDSS) and Multiple Sclerosis Functional Composite (MSFC) scores were evaluated. The individual data from all subjects are presented in table 2.

Table 2. Demographic data of the study.

Group	Subject ID	Age at baseline	Previous DMT	Gender	EDSS	MSFC	Disease time (years)
Pre Treated (PT)	1	18	Interferon $\beta$ -1a	Female	1.5	0.051	3.4
	2	24	Interferon $\beta$ -1a	Male	2.5	-0.669	9.3
	3	26	Interferon $\beta$ -1a	Female	1.5	0.494	7.2
	4	20	Interferon $\beta$ -1a	Male	1.0	1.154	0.8



	5	25	Interferon $\beta$ -1a	Female	4.5	-1.431	0.4
	6	28	Interferon $\beta$ -1a	Male	1.0	0.704	1.0
	7	30	Interferon $\beta$ -1a	Female	4.0	-0.221	6.9
	8	29	Interferon $\beta$ -1a	Male	1.0	-0,076	5.8
	9	33	Interferon $\beta$ -1a	Male	2.5	0.780	7.0
	10	46	Interferon $\beta$ -1a	Female	4.0	-0.392	1.7
	11	35	Glatiramer acetate	Male	3.5	0,311	11.2
	12	18	Interferon $\beta$ -1b	Female	0.0	-0.088	1.3
<b>Naïve (N)</b>	101	30	-	Female	0.0	0.589	0.6
	102	32	-	Male	2.5	0,061	2.3
	103	33	-	Female	5.0	-1.060	11.7
	104	22	-	Female	2.0	-0.485	0.2
	105	35	-	Female	1.0	0.188	0.4
	106	35	-	Female	5.0	-0.562	0.9
	107	44	-	Male	3.0	-0.440	5.7
	108	40	-	Male	5.0	0.469	0.6
	109	20	-	Male	1.5	1.637	0.2
	110	22	-	Female	2.0	0.045	0.6
	111	26	-	Female	4.5	-1.184	1.2
	112	20	-	Female	3.0	0.124	2.3
<b>Healthy Controls (HC)</b>	501	21	-	Male	-	-	
	502	20	-	Male	-	-	
	503	38	-	Female	-	-	
	504	33	-	Female	-	-	
	505	27	-	Male	-	-	
	506	28	-	Female	-	-	
	507	24	-	Female	-	-	
	508	36	-	Female	-	-	
	509	35	-	Female	-	-	
	510	32	-	Female	-	-	
	511	28	-	Male	-	-	
512	48	-	Female	-	-		
513	26	-	Female	-	-		

Source: The Author (2020).

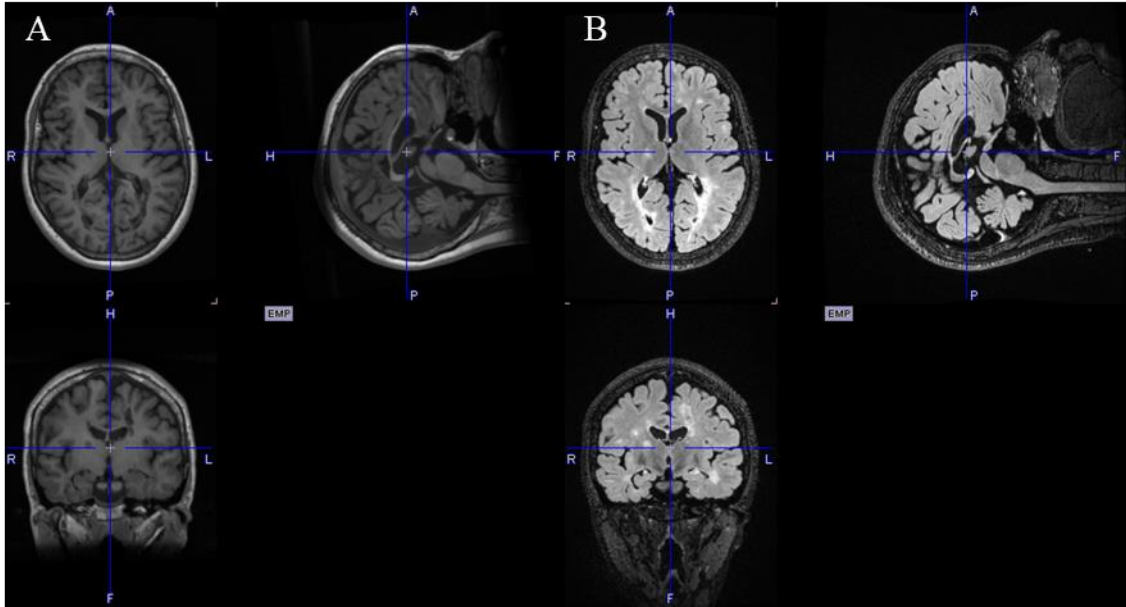
## 4.3 IMAGE ACQUISITION

### 4.3.1 MRI ACQUISITION

MR images were acquired with a GE Healthcare Signa HDxt 3.0T scanner. T1-weighted high-resolution structural images were acquired using BRAVO<sup>TM</sup> sequence (Brain Volume), with TR = 2400 ms, TE = 16 ms, FOV = 220 mm, and 1 mm isotropic voxels. T1-weighted images have a 512x512x196 pixels (240,03x240,03x196,00 mm) matrix, 16-bits per pixel, 2.133 pixels/mm resolution, 0.47x0.47x1.00 mm voxel size, and 6.12 ms

interval between frames (Figure 5A). T2-weighted images were acquired using FLAIR-3D sequence, with TR = 6000 ms, TE = 125 ms, FOV = 220 mm, and 1 mm isotropic voxels (figure 5B).

Figure 5. Example of T1 weighted MRI (A) and T2-FLAIR MRI (B) acquired in this study.



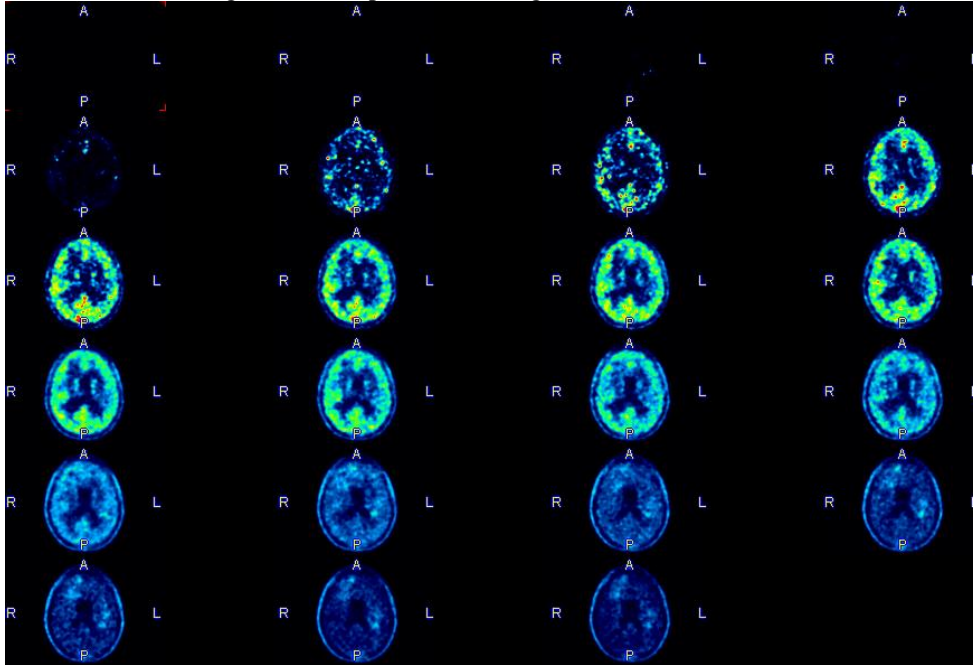
Source: The Author (2020).

#### 4.3.2 PET/CT ACQUISITION

[<sup>11</sup>C]-PK11195 PET dynamic 60-min list-mode acquisition was performed with a GE Healthcare Discovery 600 PET/CT (Time-framing: 1x15s, 3x5s, 3x10s, 2x30s, 3x60s, 4x150s, 5x300s, 2x600s) post 10kcps (Figure 6) with  $(322 \pm 106)$  MBq in the baseline,  $(279 \pm 133)$  MBq in time-point 2,  $(250 \pm 118)$  MBq in time-point 3 and  $(348 \pm 153)$  MBq in time-point 4.

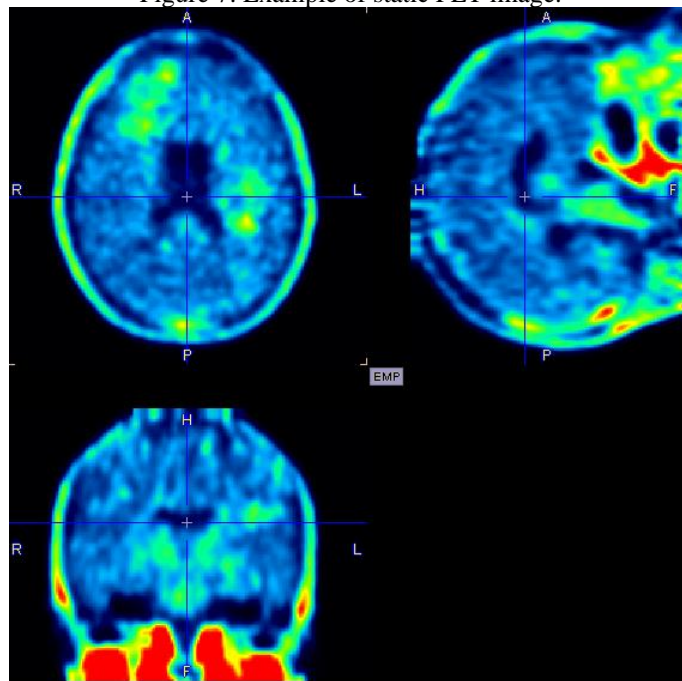
PET images were reconstructed with 300 mm FOV, using the iterative algorithm VUE Point HD®, 32 subsets, and 2 iterations, and 4.0 mm cutoff frequency smoothing filter. The image matrix has 192x192 pixels, 16-bits per pixel (0.640 pixels/mm resolution), 1.56x1.56 mm pixel size, and 47 axial slices of 3.27 mm thickness. Attenuation was corrected using CT images acquired prior to PET. Further corrections required for quantification (motion correction, normalization, decay, scatter, and random) were also applied. Static PET images were reformatted from 40-60 min post-injection (Figure 7).

Figure 6. Example of PET image with 23 time frames.



Source: The Author (2020)

Figure 7. Example of static PET image.



Source: The Author (2020)

### **4.3.3 IMAGE PROCESSING AND ANALYSIS**

#### **4.3.3.1 MRI Processing**

Four algorithms were applied to evaluate the influence of MRI segmentation method in the extracted brain volumes. MRI was segmented with fully automated methods using Statistic Parametrical Mapping (SPM8), Lesion Segmentation Tool (LST), Freesurfer and SienaX software.

Image processing was performed throughout standardized realignment, co-registration, segmentation, normalization, smoothing, and analysis contained in each software. Images and segmentation quality were visually reviewed. Next subsections present details of each segmentation method and software.

##### **4.3.3.1.1 SPM8**

SPM8 is a Matlab® application (<http://www.fil.ion.ucl.ac.uk/spm/>), developed for several brain imaging modalities, both functional, metabolic, and anatomical (fMRI, MRI, PET/CT, SPECT, EEG e MEG). WM, GM, and CSF segmentation from SPM8 are based on tissue probability maps from ICBM (International Consortium for Brain Mapping, [http://www.loni.ucla.edu/ICBM/ICBM\\_TissueProb.html](http://www.loni.ucla.edu/ICBM/ICBM_TissueProb.html)), based in T1-weighted MRI from 452 subjects in MNI space (Montreal Neurological Institute). Gaussian distributions in the source image are applied to the image segmentation in three volumes. A 4 mm spatial frequency smoothing filter and light bias regularization (0.001) parameters are used in the image pre-processing step (software standard).

##### **4.3.3.1.2 LST**

LST is a Matlab® toolbox that uses SPM8 registration, normalization, brain extraction, filtering, and analysis. Otherwise, it uses the region growth algorithm for tissue segmentation. T1w and T2-FLAIR MR images are registered and spatially normalized between both images, where the pixel value estimation is performed to create a region probability map, containing GM (pixel value =  $1.5 \leq x < 2.5$ ), WM (pixel value  $\geq 2.5$ ), and CSF (pixel value =  $0.1 \leq x < 1.5$ ). LST performs the lesion segmentation identifying low signals in T1w and high signals in T2-FLAIR MRI in the same region, using the lesion

growth algorithm. A 4mm spatial frequency smoothing filter and light bias regularization (0.001) parameters are used in the image pre-processing step (software standard).

#### 4.3.3.1.3 FreeSurfer

Freesurfer software uses an atlas that assigns classification values to WM, GM, and CSF when standardized with the input image. The atlas is based on probabilistic information on the structures positions . The statistics assigned to each tissue (averages and covariance matrices) are tabulated regionally across the atlas space, using an optimized linear algorithm to record each brain with an average value. The probabilities are computed via histogram of frequencies in the atlas space, allowing the calculation of the probability of an anatomical class to occur in a specific area of the atlas. Finally, the probability resulting from a given spatial arrangement is incorporated into the final segmentation procedure. Each probability is calculated from a training set for each point in the atlas, modelling the segmentation as a non-stationary Markov non-stationary random field (FISCHL *et al.*, 2002).

#### 4.3.3.1.4 SienaX

SienaX, implemented in FSL software, estimates brain volume from a single image (JENKINSON *et al.*, 2012; SMITH *et al.*, 2002, 2004). The first process is to separate brain tissue from the skull. The method is known as Brain Extraction Tool (BET), which uses a model that fits the brain surface, allowing deformations according to the brain regions. The images are normalized to the standard atlas MNI152 (JENKINSON; SMITH, 2001; JENKINSON *et al.*, 2002; SMITH, 2002). In the segmentation process, the model used is HMRF (Hidden Markov Random Field), and the algorithm is expectation-maximization. The image is segmented into WM, GM, CSF, and background, generating an estimate of total brain volume. SienaX segmentation includes partial volume estimation for all voxels of brain volume and not only for voxels of the brain surface. Segmentation can be performed both in the original MRI space (SienaX\_UN) and in the space normalized by the subject head size (SienaX\_NORM).

#### 4.3.3.1.5 Juxtacortical and Periventricular Segmentation

Juxtacortical and periventricular (JPV) were segmented because neuroinflammation and lesions can appear in both regions in MS (THOMPSON *et al.*, 2018). JPV regions were segmented from WM and GM provided from LST segmentation, using arithmetic and morphological operations described previously (NARCISO *et al.*, 2016). GM and WM were dilated by disk form (1 mm radius) and overlaid using an in-house script implemented in Matlab®.

#### 4.3.3.2 PET Image Processing

The head motion between PET time frames was corrected using Normalized Mutual Information in PMOD® v3.9 (PNEURO tool), with the first 15 frames (10 minutes) as reference. Registration between PET and MRI was performed in PMOD® v3.9 (PNeuro tool) with Normalized Mutual Information method, using T1-weighted MRI as reference.

Lesion masks were subtracted from WM and GM to produce the normal-appearing WM (NAWM), the normal-appearing GM (NAGM), and then summed to produce the normal-appearing whole brain without ventricles (NAWB-V) (DEBRUYNE *et al.*, 2003).

Thalamus, Putamen, Pallidum, Cerebellar GM, Cerebellar WM, Hippocampus, and Brainstem VOIs were applied to MRI with Hammers N30R83 – 1 mm atlas (HAMMERS *et al.*, 2003), and then overlapped to PET with PMOD® v3.9 (PNEURO tool).

In order to investigate [<sup>11</sup>C]-PK11195 PET quantification methods from dynamic PET data,  $V_T$  and DVR parameters were calculated using: (1) two tissue compartmental model (2TCM); (2) graphical Logan with  $t^* = 20$  min (LOG20); (3) graphical Logan with  $t^* = 40$  min (LOG40); (4) reference Logan with  $t^* = 20$  min using normal-appearing gray matter (NAGM) as reference (rLOG20-NAGM); and (5) reference Logan with  $t^* = 20$  min using normal-appearing whole-brain without ventricles (NAWB-V) as reference (rLOG20-NAWB-V).

The image-derived input function (IDIF) approach was applied in the first three methods. IDIF was extracted applying a 4 mm diameter circular ROI in the C4 portion of carotid arteries, placed manually on the PET images summed between 0 and 90 seconds, and then projected in each dynamic frame (KANG *et al.*, 2018b).

$V_T$  was calculated using LOG20 and LOG40, both using IDIF from carotid arteries (KANG *et al.*, 2018b). DVR was calculated using rLOG20-NAWB-V and rLOG20-NAGM as reference tissues (DEBRUYNE *et al.*, 2003).

In order to investigate [ $^{11}\text{C}$ ]-PK11195 PET semi-quantification methods from static PET data, SUVR was calculated for each patient in the 20 last minutes of acquisition (40-60min) (DEBRUYNE *et al.*, 2002; VERSIJPT *et al.*, 2005), using NAGM and NAWB-V as references.

#### **4.3.4 STATISTICAL ANALYSIS**

#### **4.4 MRI SEGMENTATION ANALYSIS**

Differences between brain volumes in the groups were analyzed by Student t-test, with a 95% confidence interval.

Differences between segmentation methods and software were analyzed by repeated-measures ANOVA for WM, GM, and WB, with 95% confidence interval, using covariates of gender and group (patient or control) to decrease variability impact.

To analyze the correlation between obtained data, the Intraclass Correlation Coefficient (ICC) was calculated, with a random model and two consistent factors.

The whole statistical analysis for MRI segmentation was performed using SPSS® v. 23.0.

#### **4.5 PET ANALYSIS**

$V_T$  mean differences for [ $^{11}\text{C}$ ]-PK11195 PET transversal analysis was performed with Student t-test, and the longitudinal analysis was performed with a paired t-test, both with a 95% confidence interval, using SPSS version 23.0.

SUVR and DVR mean differences for [ $^{11}\text{C}$ ]-PK11195 PET transversal analysis was performed with Student t-test using SPSS® version 23.0 and 95% confidence interval. The longitudinal analysis was performed with ANOVA for repeated measures using SPSS® version 23.0 and a 95% confidence interval.

Shapiro-Wilk normality test was performed to verify the normality of the sample for all parameters using SPSS® version 23.0 and a 95% confidence interval.

## 5 RESULTS

### 5.1 MRI SEGMENTATION

MRI segmentation was performed in four different software, SPM8, LST, FreeSurfer, and SienaX, with their respective segmentation algorithms. MR images from twenty-four MS subjects and eleven healthy controls were segmented in GM, WM, and WB. Table 3 presents GM, WM, and WB volumes obtained from each software, for both groups.

Table 3. Mean and standard deviation of the volumes segmented with different software for each group.

Region and Software	All subjects (cm <sup>3</sup> )	MS Subjects (cm <sup>3</sup> )	Controls (cm <sup>3</sup> )
<b>WM Freesurfer</b>	480 ± 51	466 ± 45	500 ± 55
<b>WM LST</b>	519 ± 69	496 ± 62	579 ± 49
<b>WM SienaX Un Norm</b>	539 ± 71	519 ± 65	582 ± 66
<b>WM SienaX Norm</b>	728 ± 59	717 ± 61	751 ± 48
<b>WM SPM8</b>	449 ± 56	433 ± 47	486 ± 59
<b>GM Freesurfer</b>	645 ± 54	639 ± 50	656 ± 62
<b>GM LST</b>	648 ± 64	631 ± 59	692 ± 61
<b>GM SienaX Un Norm</b>	606 ± 59	595 ± 53	630 ± 67
<b>GM SienaX Norm</b>	815 ± 42	817 ± 45	811 ± 28
<b>GM SPM8</b>	712 ± 81	694 ± 73	752 ± 87
<b>WB Freesurfer</b>	1115 ± 106	1096 ± 101	1155 ± 111
<b>WB LST</b>	1166 ± 120	1127 ± 105	1270 ± 97
<b>WB SienaX Un Norm</b>	1144 ± 121	1117 ± 107	1212 ± 128
<b>WB SienaX Norm</b>	1547 ± 82	1540 ± 88	1562 ± 71
<b>WB SPM8</b>	1162 ± 130	1127 ± 111	1238 ± 141

Source: The Author (2020).

The results show volumes segmented from SienaX normalized differ from all other software ( $p < 0.001$ ). Volumes segmented using SPM8 is also significantly different when compared with LST ( $p = 0.001$ ) and SienaX unnormalized ( $p = 0.001$ ) for WM, and significantly different of all other software for GM ( $p = 0.001$ ). However, SPM8 showed significant differences between WB volumes, when compared with FreeSurfer.

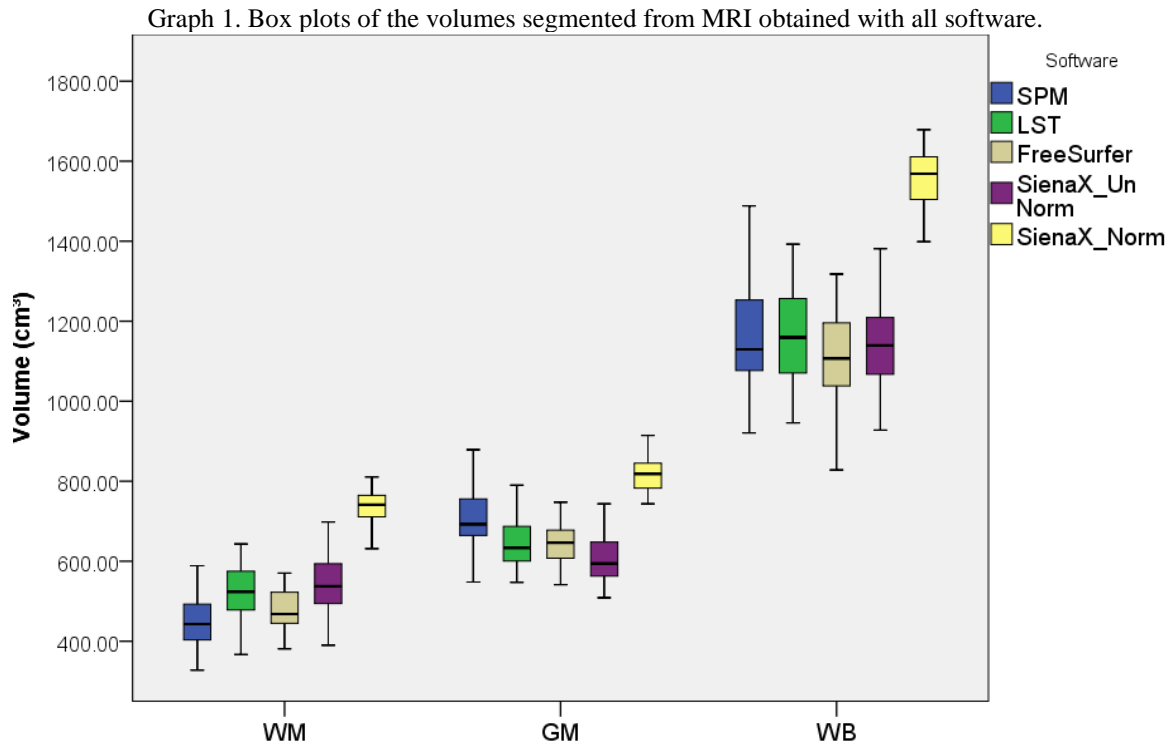
WM volume segmented from LST showed differences when compared with all software ( $p < 0.001$ ). When GM is compared with other software, LST differs from SPM8 and SienaX unnormalized ( $p = 0.001$ ). For the WB volume, LST showed differences when compared with FreeSurfer ( $p = 0.013$ ) and SienaX unnormalized ( $p = 0.027$ ).



WM volumes from FreeSurfer showed differences when compared with LST ( $p < 0.001$ ) and SienaX unnormalized ( $p < 0.001$ ). GM from FreeSurfer is different when compared with SPM8 ( $p < 0.001$ ) and SienaX unnormalized ( $p < 0.001$ ). For WB volumes, FreeSurfer differ from SPM8 ( $p = 0.034$ ) and LST ( $p = 0.013$ ).

SienaX unnormalized also showed differences for WM and GM volumes when compared with all software ( $p < 0.001$ ). For WB, as mentioned before, differences are only presented for LST ( $p = 0.027$ ).

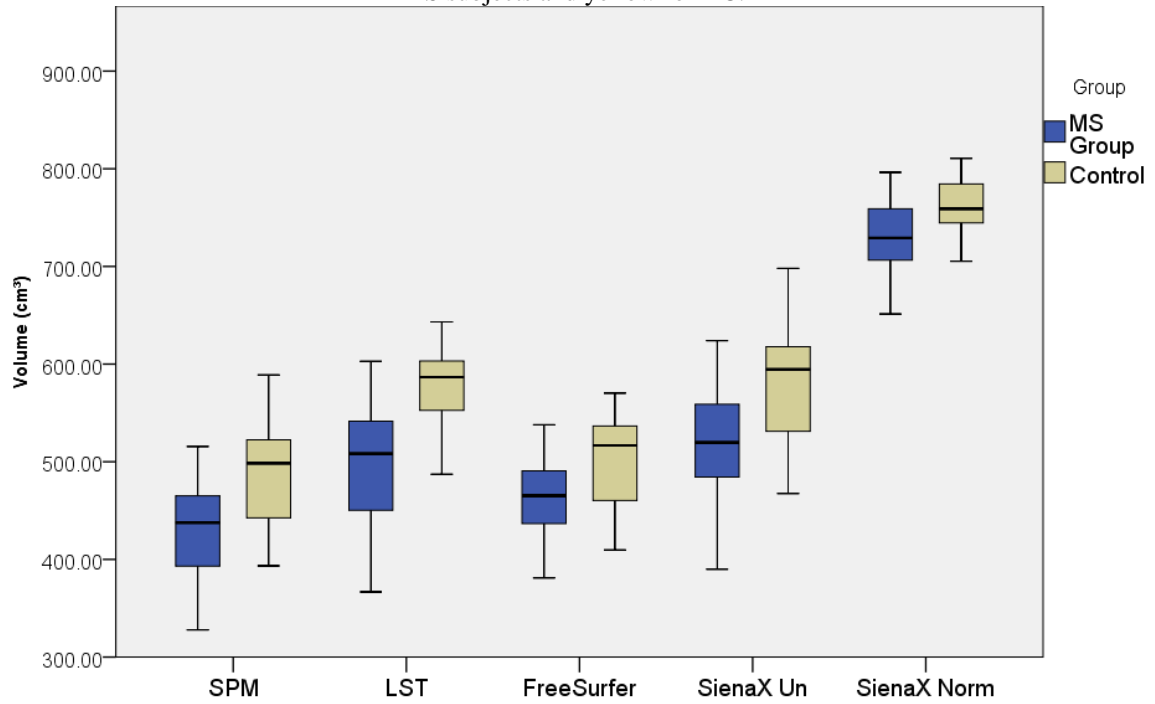
Graph 1 shows the comparison of the volume for each VOI and each software. All box plots, in this work, have the median as the the thick line in the middle of the box. The top and bottom box lines are the first and third quartiles, and the whiskers show the maximum and minimum values, with the exceptions of outliers (circles).



Source: The Author (2020).

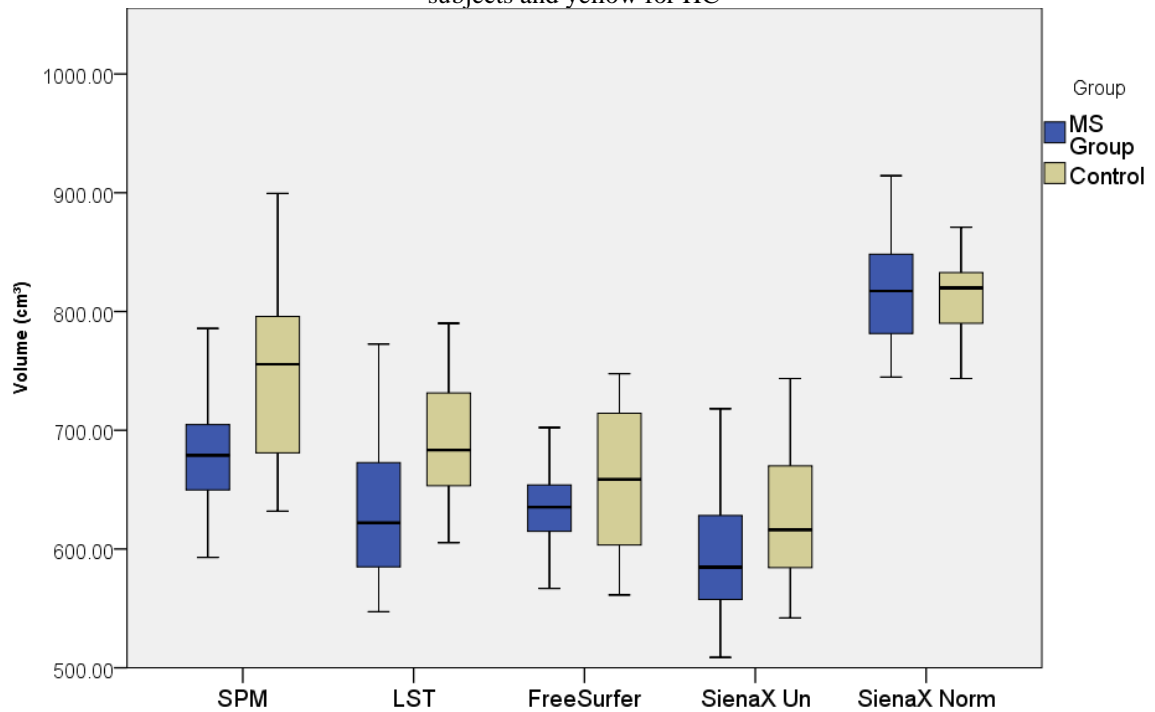
Healthy controls have WM volume significantly higher than MS subjects when segmented in SPM8 ( $p = 0.008$ ), LST ( $p = 0.001$ ) and SienaX unnormalized ( $p = 0.012$ ) (Graph 2), and GM volumes significantly higher than MS subjects when segmented from SPM8 ( $p = 0.046$ ) and LST ( $p = 0.013$ ) (Graph 3).

Graph 2. Box plots of WM volumes segmented for each software per group. In blue the WM volumes for MS subjects and yellow for HC.



Source: The Author (2020).

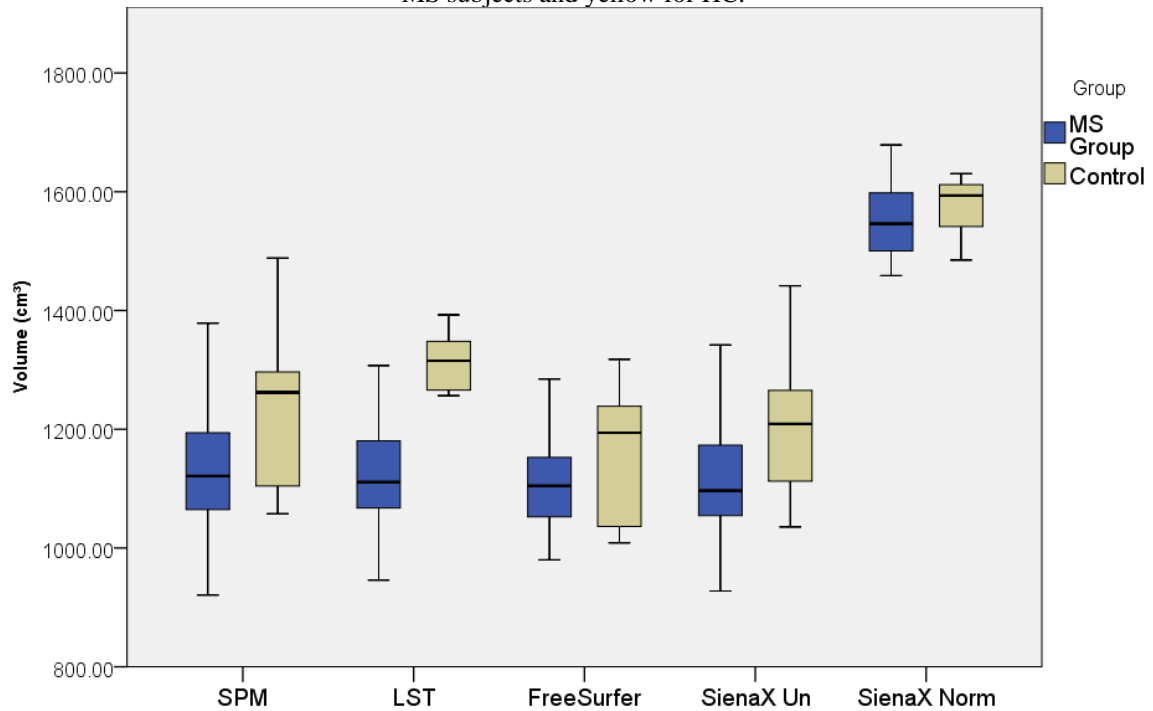
Graph 3. Box plots of GM volumes segmented for each software per group. In blue the GM volumes for MS subjects and yellow for HC



Source: The Author (2020).

WB volumes are significantly higher in healthy controls than MS subjects, segmented using SPM8 ( $p = 0.016$ ), LST ( $p = 0.001$ ) and SienaX unnormalized ( $p = 0.024$ ) (Graph 3).

Graph 4. Box plots of WB volumes segmented for each software per group. In blue the WM volumes for MS subjects and yellow for HC.



Source: The Author (2020).

The inter-class correlation (ICC) was calculated between groups. Correlation variates from strong for the WM and moderate for the GM and WB, when comparing all software. When volumes segmented using SienaX normalized were withdrawn from the analysis, ICC presents strong correlation between all software, resulting in  $ICC(WM) = 0.857$ ;  $ICC(GM) = 0.857$  and;  $ICC(WB) = 0.864$ .

## 5.2 DYNAMIC PET QUANTIFICATION

This part of the study aims to investigate quantification methods from dynamic [ $^{11}C$ ]-PK11195 PET data to understand and explain the longitudinal behavior in MS subjects and the differences from healthy subjects. In the next sub-section, the results of the following methods are presented: IDIF and reference tissue modelling.

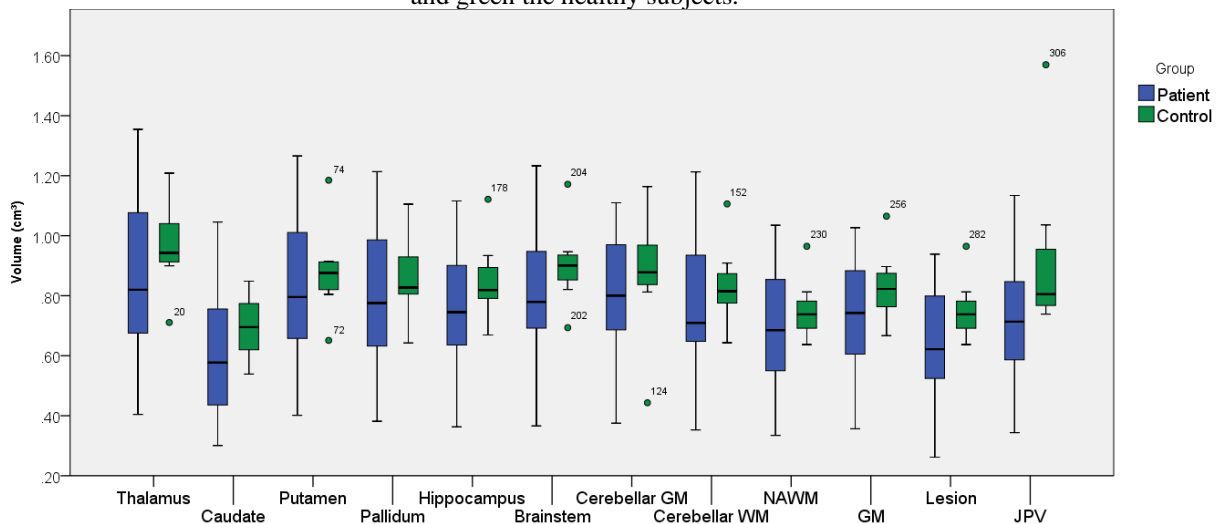
## 5.2.1 IMAGE DERIVED INPUT FUNCTION

The first [ $^{11}\text{C}$ ]-PK11195 PET quantification method was performed using the IDIF extracted from carotid arteries in MRI. This analysis aims to investigate the  $V_T$  behavior when IDIF is applied in cortical and subcortical VOIs quantification. For the transversal analysis, PET images from eighteen MS subjects (including PT and N subjects) and eight healthy controls (HC) were used. For the longitudinal analysis, PET images from nine MS naïve subjects (N) were used. Three kinetic models were applied: 2TCM, LOG20, and LOG40. The kinetic parameter  $V_T$  was extracted from the thalamus, caudate, putamen, pallidum, hippocampus, brainstem, cerebellar GM and WM, NAWM, GM, lesions, and JPV. Results are described in the next three sub-sections.

### 5.2.1.1 2TCM – Transversal Analysis

$V_T$  values determined from 2TCM per group (MS and HC) are presented in Graph 5. No statistical differences in  $V_T$  were found for any VOI between the MS and HC groups. Even after withdrawing the outliers, this result remains the same.

Graph 5. Box plot of  $V_T$  determined from 2TCM per group (transversal analysis). In blue the MS subjects and green the healthy subjects.



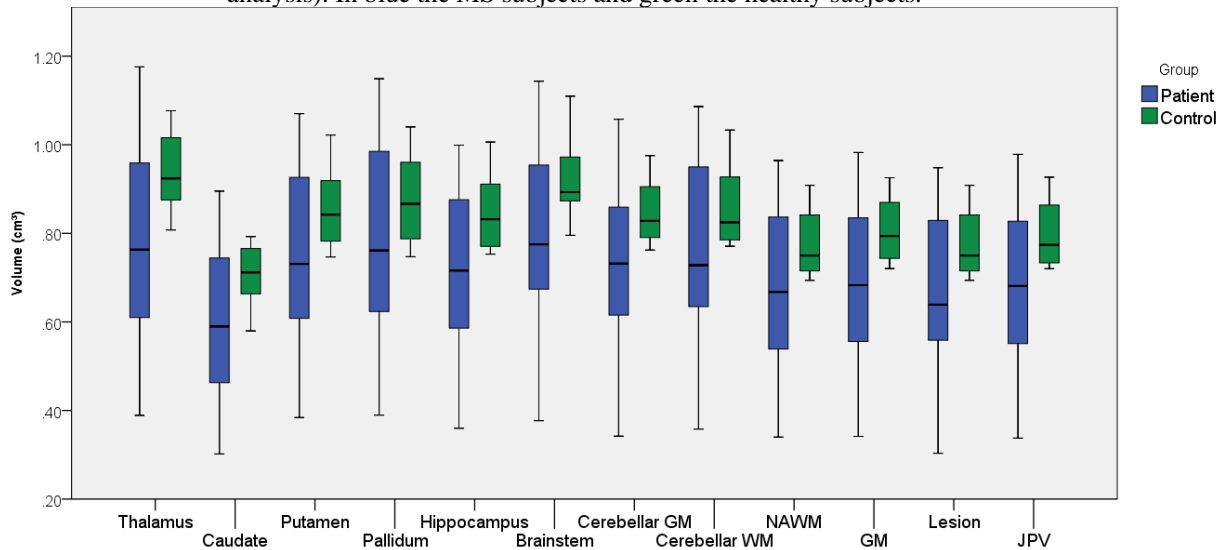
Source: The Author (2020).

### 5.2.1.2 Graphical Logan Model – Transversal Analysis

#### 5.2.1.2.1 Logan ( $t^*=20min$ ) – Transversal Analysis

$V_T$  values determined from LOG20 are presented in Graph 6. No statistical differences between  $V_T$  were found between MS and HC subjects. No outliers were found in this quantification method in the transversal analysis.

Graph 6. Box plot of  $V_T$  determined from the graphical Logan model ( $t^* = 20$  min) per group (transversal analysis). In blue the MS subjects and green the healthy subjects.

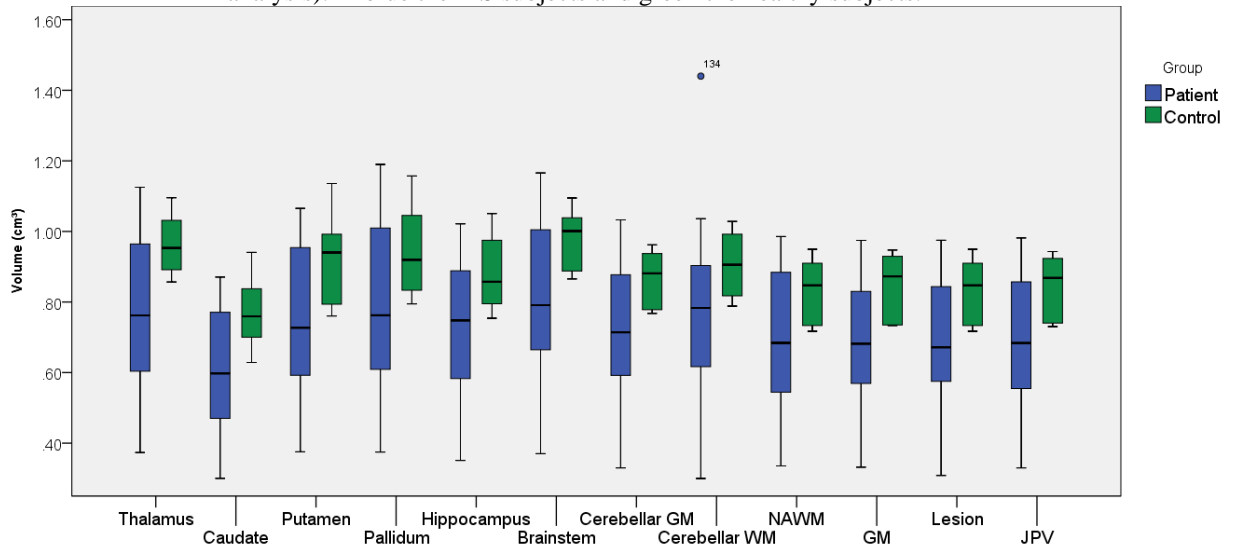


Source: The Author (2020).

#### 5.2.1.2.2 Logan ( $t^*=40min$ ) – Transversal Analysis

Using LOG40,  $V_T$  values showed statistical differences between MS and HC groups in the following regions: caudate (MS =  $0.61 \pm 0.18$ ; HC =  $0.77 \pm 0.10$ ;  $p=0.026$ ), GM (MS =  $0.69 \pm 0.18$ ; HC =  $0.84 \pm 0.10$ ;  $p=0.035$ ), cerebellar GM (MS =  $0.72 \pm 0.19$ ; HC =  $0.87 \pm 0.08$ ;  $p=0.041$ ), thalamus (MS =  $0.78 \pm 0.22$ ; HC =  $0.96 \pm 0.09$ ;  $p=0.041$ ), putamen (MS =  $0.75 \pm 0.21$ ; HC =  $0.91 \pm 0.13$ ;  $p=0.046$ ), brainstem (MS =  $0.80 \pm 0.22$ ; HC =  $0.98 \pm 0.09$ ;  $p=0.046$ ), and JPV (MS =  $0.70 \pm 0.19$ ; HC =  $0.84 \pm 0.09$ ;  $p=0.049$ ). No statistical differences in  $V_T$  were found in Pallidum, Hippocampus, Cerebellar WM, NAWM and Lesions. Graph 7 shows the distribution of  $V_T$  per group. Caudate showed the highest statistical difference in  $V_T$  when MS and HC subjects are compared, which agrees with the hypothesis that demyelination can occur in subcortical GM, in agreement with previous studies using ultra-high-field MRI (PITT *et al.*, 2010).

Graph 7. Box plot of  $V_T$  determined from the graphical Logan model ( $t^* = 40$  min) per group (transversal analysis). In blue the MS subjects and green the healthy subjects.



Source: The Author (2020).

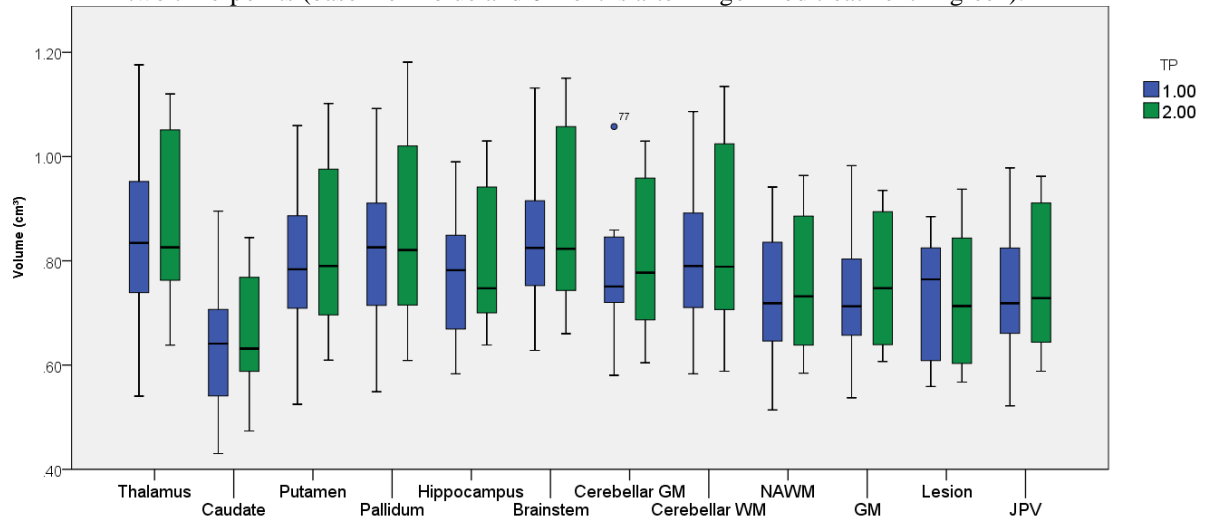
### 5.2.1.3 Logan Graphical Model – Longitudinal Analysis

Both the LOG20 and LOG40 were also applied to investigate longitudinal differences in  $^{11}\text{C}$ -PK11195 uptake, in the 2 first time-points for MS naïve subjects, in order to observe the impact of fingolimod treatment after 6 months in  $V_T$  values.

#### 5.2.1.3.1 Logan ( $t^*=20\text{min}$ )

$V_T$  values determined from LOG20 in the longitudinal analysis are presented in Graph 8. No statistical differences in  $V_T$  between the baseline and after 6 months of fingolimod treatment in MS naïve subjects were found. After withdrawing outliers, the results remain the same.

Graph 8. Box plot of  $V_T$  determined from the graphical Logan model ( $t^* = 20$  min) for MS naïve subjects in two time-points (baseline in blue and 6 months after fingolimod treatment in green).

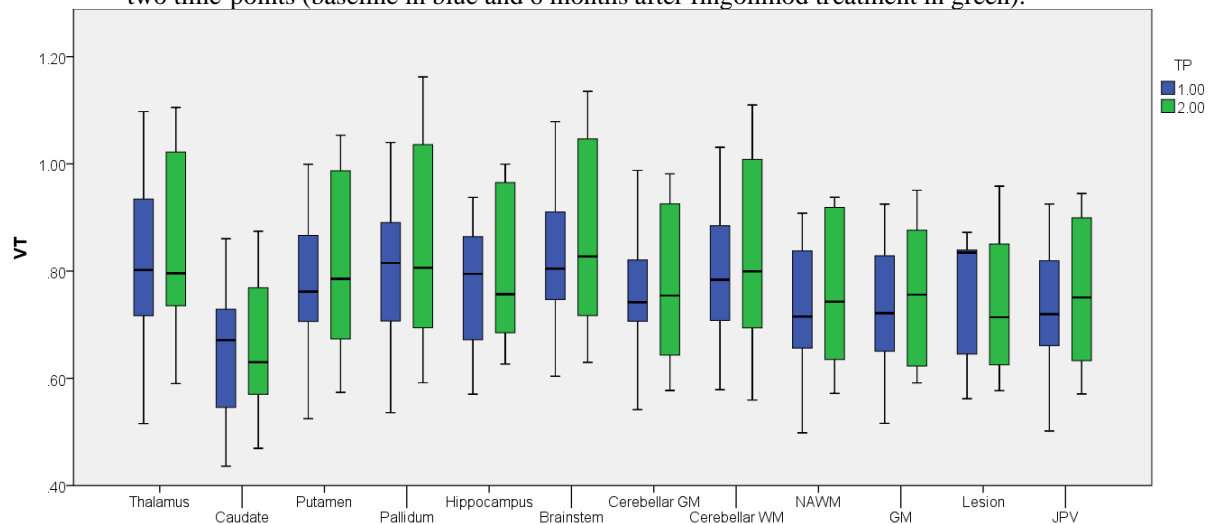


Source: The Author (2020).

#### 5.2.1.3.2 Logan ( $t^*=40min$ )

$V_T$  values determined from LOG40 in the longitudinal analysis are presented in Graph 9. No statistical differences in  $V_T$  between the baseline and after 6 months of fingolimod treatment in MS naïve subjects were found. After withdrawing outliers, the results remain the same.

Graph 9. Box plot of  $V_T$  determined from the graphical Logan model ( $t^* = 40$  min) for MS naïve subjects in two time-points (baseline in blue and 6 months after fingolimod treatment in green).



Source: The Author (2020).

It is possible to observe that the IDIF approach produces a high  $V_T$  variability. The method that better differ MS and HC groups is the LOG40. However,  $V_T$  is higher in HC than in subjects, which does not match with the literature (GIANNETTI *et al.*, 2014; KANG

*et al.*, 2018a; KAUNZNER *et al.*, 2017, 2019; POLITIS *et al.*, 2012; RATCHFORD *et al.*, 2012; RISSANEN *et al.*, 2014, 2018; SUCKSDORFF *et al.*, 2017). Possibly this can be due to the high uptake present in the epithelial tissue that surrounds portion C4 of carotid arteries in PET images. The reference tissue approach was used to overcome this pitfall to evaluate the [<sup>11</sup>C]-PK11195 PET kinetic behavior.

## **5.2.2 REFERENCE TISSUE MODELLING**

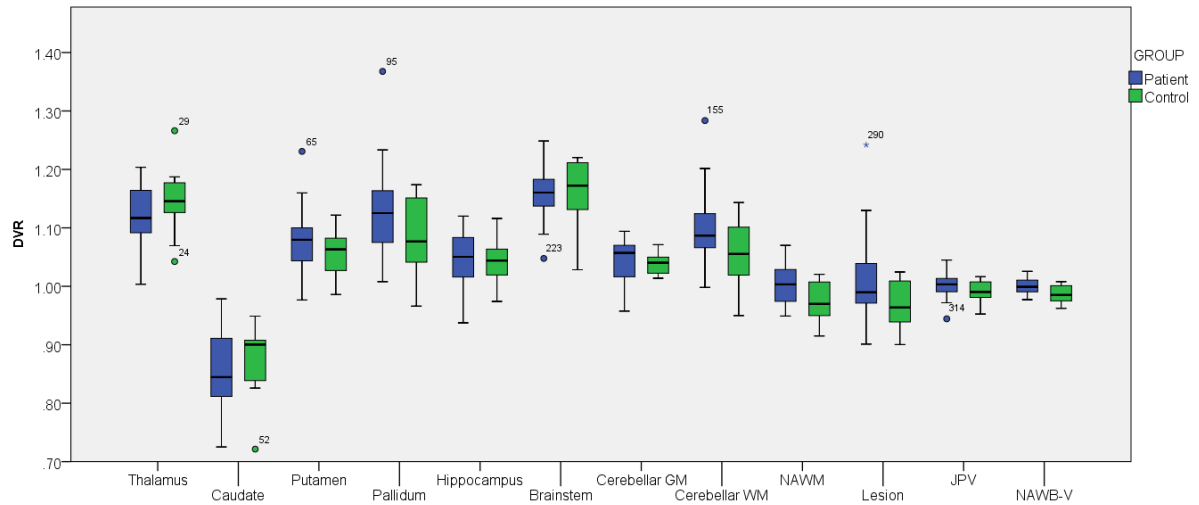
The second [<sup>11</sup>C]-PK11195 PET quantification method was performed using a reference tissue as input function. DVR behavior using a reference tissue modelling was applied in cortical and subcortical VOIs quantification. Reference Logan model ( $t^*=20$ ) and two reference tissues, NAGM and NAWB-V, were evaluated. The transversal analysis used dynamic PET data extracted from twenty-one MS subjects (10 PT + 11 N) and eight HC, and DVR calculated using NAGM and NAWB-V as reference tissues. The longitudinal analysis used dynamic PET from nine pre-treated MS subjects (PT) and 8 naïve subjects (N) in four time-points (baseline, 6 months, 12 months, and 24 months) to observe the DVR behavior after fingolimod treatment initiation. Results are described in the next three sub-sections.

### **5.2.2.1 Reference Logan with NAGM as reference ( $t^*=20$ min) - Transversal Analysis**

DVR values in the transversal analysis using rLOG20-NAGM are presented in Graph 10. No statistical differences were found between DVR in MS and HC subjects. After withdrawing outliers, the results remain the same.



Graph 10. Box plot of DVR determined from the reference Logan model ( $t^* = 20$  min) using NAGM as the reference, per group (transversal analysis).

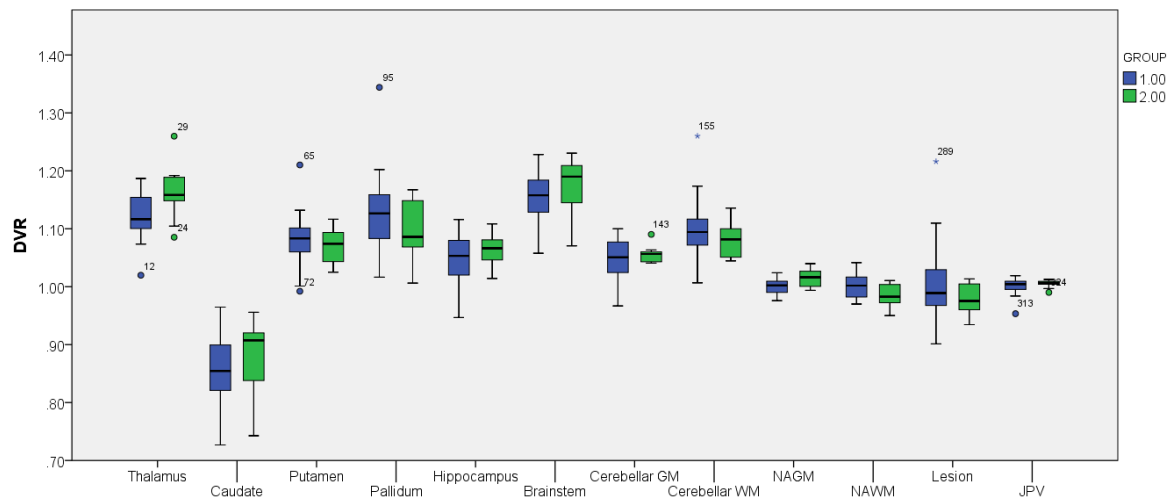


Source: The Author (2020).

### 5.2.2.2 Reference Logan with NAWB-V as the reference ( $t^*=20$ min) - Transversal Analysis

DVR values in the transversal analysis using the rLOG20- NAWB-V are presented in Graph 11. Statistical differences between MS subjects and HC were found in the following VOIs: thalamus (MS =  $1.12 \pm 0.04$ ; HC=  $1.16 \pm 0.05$ ;  $p=0.033$ ), NAWM (MS =  $1.00 \pm 0.02$ ; HC=  $0.97 \pm 0.02$ ;  $p=0.034$ ), and NAGM (MS =  $1.00 \pm 0.01$ ; HC=  $1.02 \pm 0.02$ ;  $p=0.022$ ). No statistical differences in DVR were found in Caudate, Putamen, Pallidum, Hippocampus, Brainstem, Cerebellar GM, Cerebellar WM, JPV and NAWB.

Graph 11. Box plot of DVR determined from the reference Logan model ( $t^* = 20$  min) using NAWB-V as the reference, per group (transversal analysis). In blue the MS subjects and green the healthy subjects.

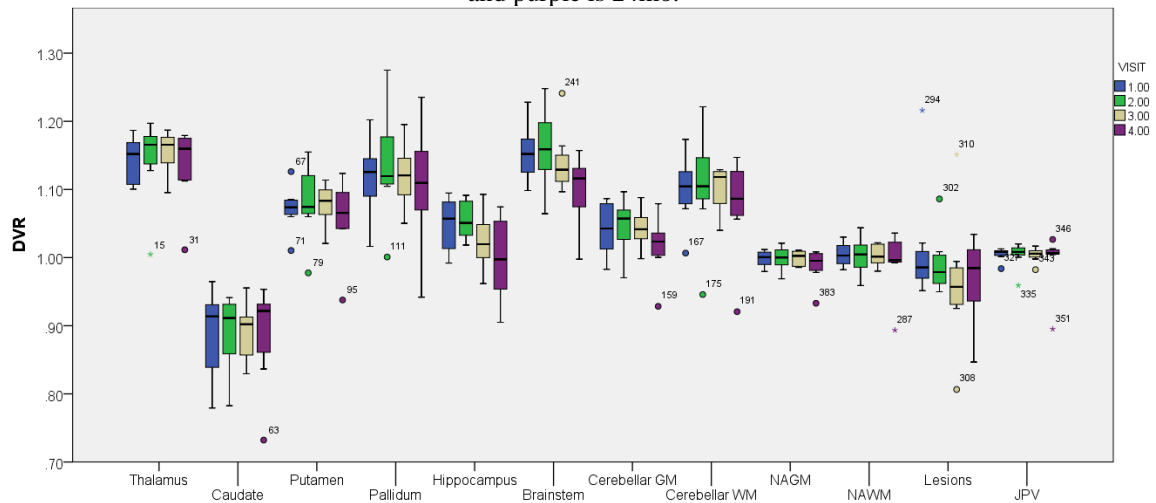


Source: The Author (2020).

### 5.2.2.3 Reference Logan with NAWB-V as the reference (t\*=20min) - Longitudinal Analysis

DVR values in the longitudinal analysis using the rLOG20-NAWB-V are presented in Graph 12. Microglial activation assessed with [<sup>11</sup>C]-PK11195 shows a statistical significantly decrease in DVR for naïve MS subjects between the baseline (0 months) and the 4th time-point (24 months) in hippocampus (p = 0.005) and brainstem (p = 0.008), and between the 2<sup>nd</sup> (6 months) and 4th time-point (24 months) in the cerebellar GM (p = 0.011), hippocampus (p = 0.029) and brainstem (p = 0.003).

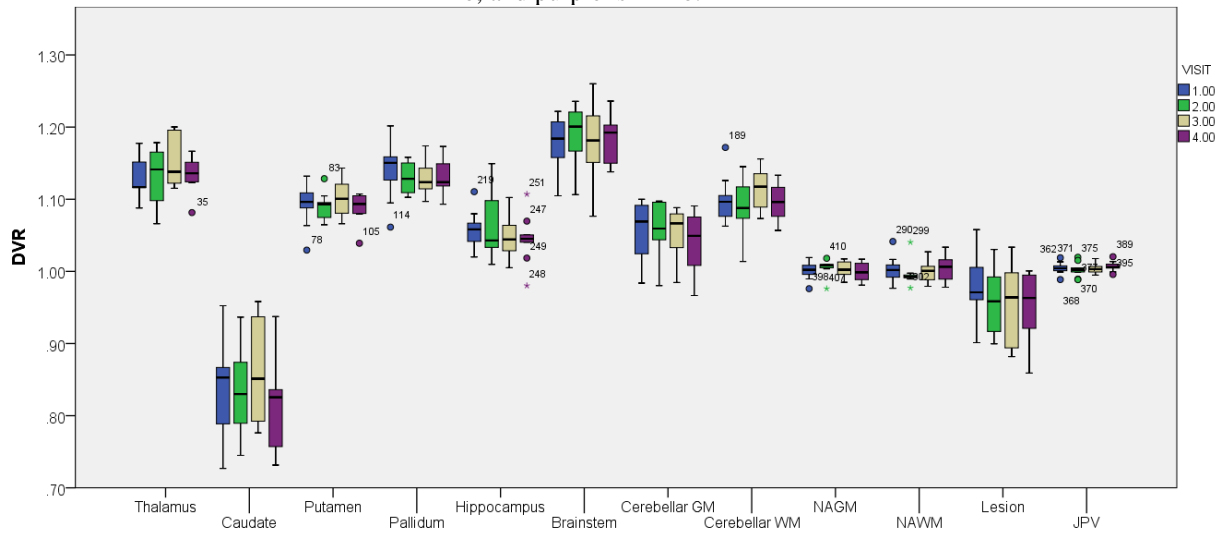
Graph 12. Box plot of DVR determined from the reference Logan model (t\* = 20 min) using NAWB-V as the reference, in naïve MS subjects (longitudinal analysis). Blue is baseline, green is 6mo, beige is 12mo, and purple is 24mo.



Source: The Author (2020).

Although analyzing only the pre-treated MS subjects (PT), DVR increases in the thalamus (p = 0.018) region from the baseline (0 months) to the 3<sup>rd</sup> time-point (12 months).

Graph 13. Box plot of DVR determined from the reference Logan model ( $t^* = 20$  min) using NAWB-V as the reference, in pre-treated MS subjects (longitudinal analysis). Blue is baseline, green is 6mo, beige is 12 mo, and purple is 24mo.



Source: The Author (2020).

The [ $^{11}\text{C}$ ]-PK11195 PET quantification using the reference tissue modelling shows a decrease of DVR variability using both methods DVR with NAGM, and with NAWB-V as references. However, the method that could better distinguish MS subjects and HC was the rLOG20-NAWB-V as reference. This method was chosen to produce a longitudinal analysis. In the longitudinal analysis, a decrease in DVR is observed in hippocampus and brainstem between the baseline and 4<sup>th</sup> time-point, and in the cerebellar GM, hippocampus, and brainstem between the 2<sup>nd</sup> and 4<sup>th</sup> time-point. This result could suggest a decrease in neuroinflammation due to the fingolimod treatment intervention.

### 5.3 STATIC PET SEMI-QUANTIFICATION

This part of the study aimed to investigate semi-quantification methods from static [ $^{11}\text{C}$ ]-PK11195 PET data to understand and explain the longitudinal behavior in MS subjects and the differences from healthy subjects. The static PET image was reformatted from dynamic PET data between 40min and 60 min, post 10kcp.

SUVr was applied to cortical and subcortical VOI quantification using NAGM and NAWB-V regions as references. SUVr (NAGM) and SUVr (NAWB-V) were used to analyze the differences between twenty-one MS subjects (10 pre-treated and 11 naïve) and nine HC. The SUVr with NAWB-V as reference was used to analyze PET data from nine pre-treated MS subjects and 8 naïve subjects in 4 time-points longitudinally, in order to

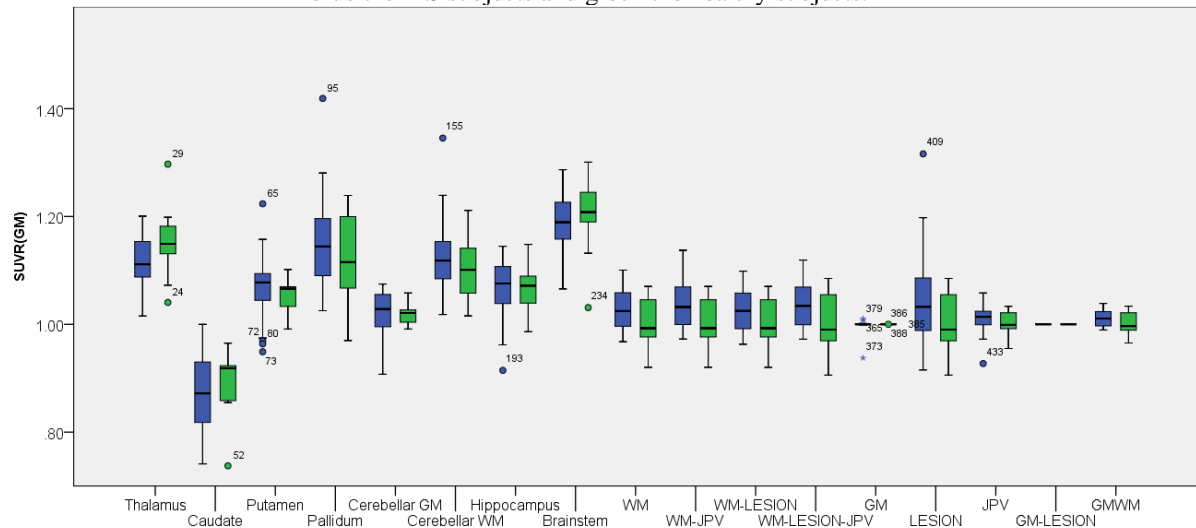
study SUVR behavior after fingolimod treatment initiation. The results are described in the next three sub-sections.

### 5.3.1 SUVR WITH NAGM AS REFERENCE

#### 5.3.1.1 Transversal Analysis

SUVR values using NAGM as the reference in transversal analysis between MS and HC subjects are presented in Graph 14. No statistical differences in SUVR (NAGM) were found in the VOIs between MS subjects and HC groups. After withdrawing outliers, the results remain the same.

Graph 14. Box plot of SUVR using NAGM as the reference, in MS subjects and HC (transversal analysis). In blue the MS subjects and green the healthy subjects.

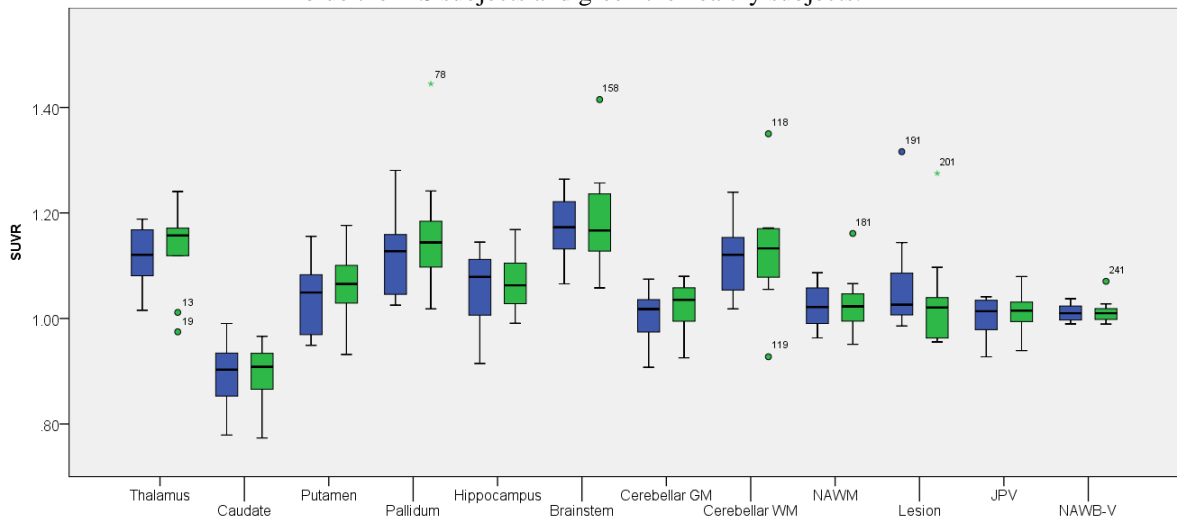


Source: The Author (2020).

#### 5.3.1.2 Longitudinal Analysis

SUVR values using NAGM as the reference in longitudinal analysis for naïve MS subjects are presented in Graph 15. Statistically significant decrease SUVR in lesions were found between the baseline and the 2<sup>nd</sup> time-point (6 months) ( $V1 = 1.07 \pm 0.10$ ;  $V2 = 1.03 \pm 0.09$ ;  $p=0.008$ ). After withdrawing outliers, the results remain the same.

Graph 15. Box plot of SUVR using NAGM as the reference, in naïve MS subjects (longitudinal analysis). In blue the MS subjects and green the healthy subjects.



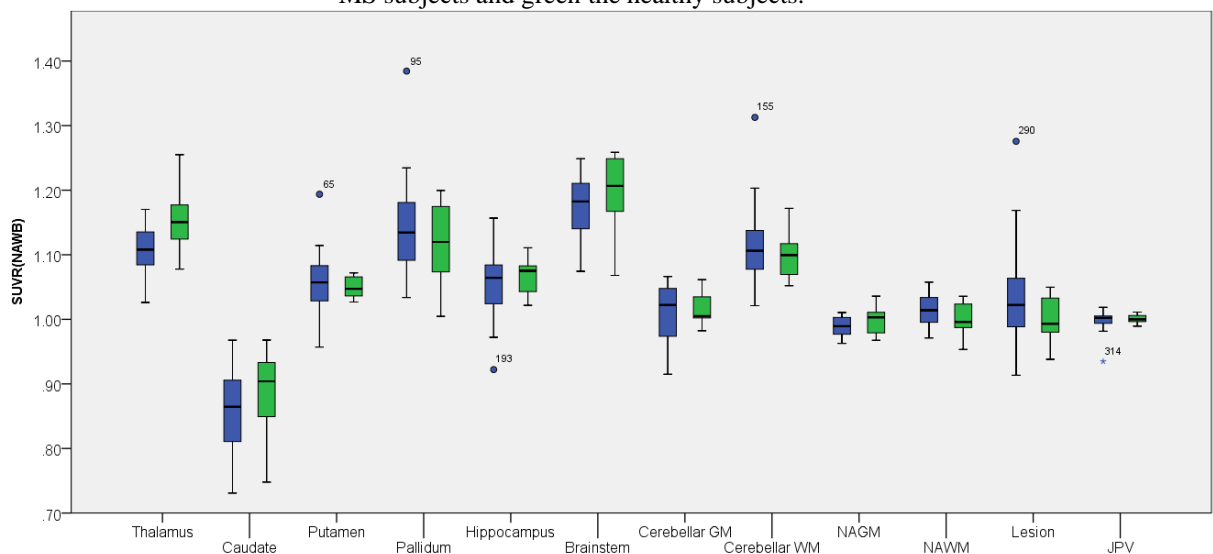
Source: The Author (2020).

### 5.3.2 SUVR WITH NAWB-V AS REFERENCE

#### 5.3.2.1 Transversal Analysis

SUVR values using NAWB-V as the reference in transversal analysis between MS and HC subjects are presented in Graph 16. A statistically significant difference between MS and HC subjects in SUVR was found in thalamus (MS=  $1.11 \pm 0.04$ ; HC=  $1.15 \pm 0.05$ ;  $p=0.014$ ). No statistical differences in SUVR(NAWB-V) were found in other regions. After withdrawing outliers, the results remain the same.

Graph 16. Box plot of SUVR using NAWB-V as the reference, per group (transversal analysis). In blue the MS subjects and green the healthy subjects.

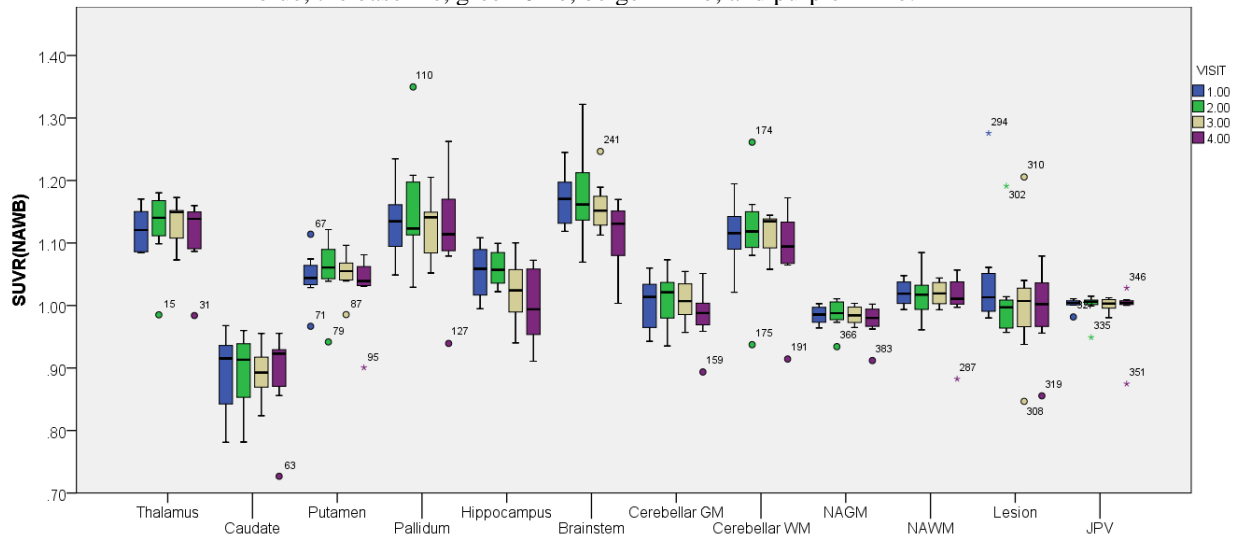


Source: The Author (2020).

### 5.3.2.2 Longitudinal Analysis

Microglial activation assessed with [<sup>11</sup>C]-PK11195 PET shows a statistical significant decrease in SUVR(NAWB-V) for naïve MS subjects between baseline and 4<sup>th</sup> time-point (24 months) in hippocampus (p = 0.003) and brainstem (p = 0.021), and between the 2<sup>nd</sup> (6 months) and 4<sup>th</sup> time-point (24 months) in hippocampus (p = 0.012), brainstem (p = 0.017) and putamen (p = 0.044). All data is present in the box plot for both methods.

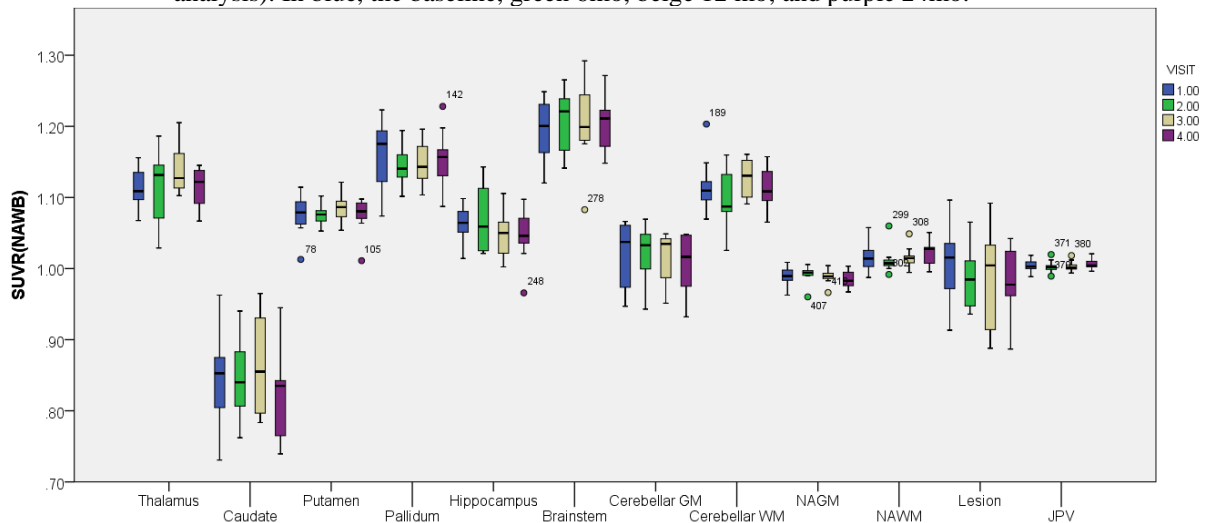
Graph 17. Box plot of SUVR using NAWB-V as the reference, in naïve MS subjects (longitudinal analysis). In blue, the baseline, green 6mo, beige 12 mo, and purple 24mo.



Source: The Author (2020).

Although, for pre-treated MS subjects, SUVR(NAWB-V) increased in the thalamus (p = 0.012) region between the 1<sup>st</sup> time-point (baseline) to the 3<sup>rd</sup> time-point (12 months). The other regions did not show any differences between time-points.

Graph 18. Box plot of SUVR using NAWB-V as the reference, in pre-treated MS subjects (longitudinal analysis). In blue, the baseline, green 6mo, beige 12 mo, and purple 24mo.



Source: The Author (2020).

The [<sup>11</sup>C]-PK11195 PET quantification using SUVR shows a decrease in variability using both references, NAGM and NAWB-V. However, the method that could better distinguish MS subjects and HC was the SUVR with NAWB-V as the reference. The last method was chosen to analyze the longitudinal data. In the longitudinal analysis, a decrease in SUVR is observed in hippocampus and brainstem between the baseline, and 4<sup>th</sup> time-point, and in the putamen, hippocampus, and brainstem between the 2<sup>nd</sup> and 4<sup>th</sup> time-point. This result could suggest a decrease in neuroinflammation due to the fingolimod treatment intervention.

## 6 DISCUSSION

### 6.1 MRI SEGMENTATION

In this study, the brain regions segmentation, such as GM, WM, lesions, is a critical step required for PET quantification. The segmentation allows the evaluation of GM and WM volumes, which aid in the diagnosis of several brain diseases, among which Alzheimer's disease (AD), mild cognitive impairment (MCI), and multiple sclerosis (MS). MRI techniques permit to better discriminate between GM and WM. It also provides the visualization of GM lesions *in vivo* and to quantify structural and functional damage of the cortical and subcortical GM (FELLHAUER *et al.*, 2015; POLMAN *et al.*, 2011; SCHMIDT *et al.*, 2012).

Different algorithms have been developed to segment automatically MRI brain regions. Automated segmentation methods assume the time-consuming manual segmentation method of tissue classification. In MRI acquisition, noise, or inhomogeneity in the image data frequently occurs. These interferences may affect the automatic segmentation methods and thus, alter the results of the brain volumes measurement. Therefore, the segmentation algorithms have to be robust to provide reliable results. However, studies comparing the reliability of these segmentation algorithms are scarce and mainly involved MRI derived from young healthy controls.

FELLHAUER *et al.* (2015) evaluated GM and WM volumes from AD, MCI, and healthy subjects using four algorithms: SPM8, SPM12, FreeSurfer, and SienaX. This study showed that the automated segmentation methods have difficulties to correctly classify the brain tissue, especially with increasing image noise. They showed that increasing noise affected the FreeSurfer segmentation of GM, but had no negative effect on the segmentation results of WM. SPM algorithms provide more stable results with increasing noise, and strong field inhomogeneity has almost no effect on the segmentation. With increasing noise SPM tends to underestimate GM and overestimate WM, as well as SienaX. The analysis of the AD and MCI data yielded decreasing volumes of GM and WM with the progression of brain atrophy independent of the algorithm used. FreeSurfer calculated the largest GM and the smallest WM volumes. SienaX calculated the smallest GM volumes; SPM the largest WM volumes.



Analyzing Graph 1 is possible to observe that our data follows the same behavior of previous studies (FELLHAUER *et al.*, 2015), where SienaX without spatial normalization gives the smallest volumes of GM. SienaX normalized by the subject's head size provides slightly higher volumes than SienaX unnormalized. Considering all other algorithms use the original MRI space for volume estimation, SienaX normalized is not indicated for comparative studies, due to the spatial normalization using MNI space, which deforms the brain regions and might provide wrong analysis.

Oppositely from previous studies, SPM showed higher variability in volume data compared with LST (FELLHAUER *et al.*, 2015). According to our results, LST is recommended for structural brain volume analysis of MS subjects, since it provides overall good segmentation results even in more difficult measurement situations, especially concerning small lesions, motion, and inhomogeneities. LST advantages might be assumed due to the use of all benefits of SPM8 image pre-processing parameters and transformation, with the benefit of using two different MRI weighting (T1-weighted and T2-FLAIR).

Regarding the chosen statistical model to analyze the data, repeated measures ANOVA is a susceptible statistic test for relatively small samples, which can give overestimated statistical significance in other software comparisons. Also, the volume variability could be increased because the WM and GM tissues of MS subjects present lesions and abnormalities induced by MS.

In this work, segmentation from LST was employed to PET quantification due to its lower variability when compared with the other software and the use of two types of MRI (T1-weighted and T2-FLAIR) in the segmentation process.

## **6.2 DYNAMIC PET QUANTIFICATION**

In this study, we aimed to investigate two kinetic parameters,  $V_T$  and DVR, in MS and healthy subjects in transversal and longitudinal studies. Two fully quantitative methods were applied to dynamic PET images, the first using IDIF to calculate  $V_T$ , and the second using the reference tissue modelling to determine DVR. In the first quantitative method the 2TCM, LOG20, and LOG40 were used. In the second quantitative method, the reference Logan model was used with NAGM and NAWB-V as references.

Using IDIF, LOG40 is capable of differentiating  $V_T$  from MS subjects and healthy controls in the transversal analysis. However,  $V_T$  from MS subjects was lower than HC, which did not agree with previous studies, that shows  $V_T$  higher in MS subjects when compared with healthy subjects (KANG *et al.*, 2018a; POLITIS *et al.*, 2012; RISSANEN *et al.*, 2014, 2018; SUCKSDORFF *et al.*, 2017). This result could be related to the carotid C4 portion is surrounded by epithelial tissue, which has a high affinity to [ $^{11}\text{C}$ ]PK11195. The inclusion of the epithelial tissue uptake in the ROI delineation of the carotid can produce an overestimation in the blood activity concentration. Considering the blood concentration corresponds to the term  $C_P$  in equation 5, its increase can result in a  $V_T$  underestimation in MS subjects with microglial activation, when compared to HC. Further studies are required to ensure the exclusion of the epithelial tissue in the carotid segmentation in IDIF.

The  $V_T$  overestimation in MS subjects, when compared with healthy subjects, is also observed for 2TCM and LOG20. Nevertheless, both methods are not able to differentiate  $V_T$  from MS subjects and healthy controls. None of the methods was able to indicate  $V_T$  differences between the naïve baseline and 6 months after fingolimod initiation. Some refinements in IDIF methods presented in previous studies are population-based metabolites and partial volume corrections (KANG *et al.*, 2018b, 2018c; ROIVAINEN *et al.*, 2009). However, in this study, we did not perform these corrections due to the lack of metabolites analysis.

Using GM as reference tissue, rLOG20 does not show differences in DVR between MS subjects and healthy subjects. Although, DVR in all regions is higher for MS subjects than in healthy controls, which agrees with previous studies (KANG *et al.*, 2018a; RISSANEN *et al.*, 2014; SUCKSDORFF *et al.*, 2017). DVR values for both MS subjects and HC show more reliable results with lower variability when compared to  $V_T$ .

A decrease in DVR in the MS lesions is identified in naïve subjects after 6 months of treatment initiation, using rLOG20-NAGM, which agrees with previous MS longitudinal studies (RATCHFORD *et al.*, 2012; SUCKSDORFF *et al.*, 2017). This result could indicate a positive fingolimod treatment effect in MS for the naïve MS subjects. The decrease in lesion uptake did not happen in the pre-treated group. The uptake decrease could be associated with the low uptake in chronic lesions, which are not separated from active lesions in MRI segmentation, agreeing with a previous study (KAUNZNER *et al.*, 2017).

Further studies are required to investigate if there is a correlation between active lesions in gadolinium-enhanced MRI and [ $^{11}\text{C}$ ]-PK11195 PET quantification.

In this study, an alternative approach was used for [ $^{11}\text{C}$ ]-PK11195 PET quantification, using the NAWB-V as the reference tissue. This approach was based on the lack of a standardized reference region. Two published studies disagree in choosing a reference tissue, one uses GM as the reference (KAUNZNER *et al.*, 2019), while the other uses WM (RISSANEN *et al.*, 2018). Our approach using DVR from rLOG20-NAWB-V as reference tissue is capable of differentiating MS and healthy subjects. Moreover, a DVR decrease is observed for the hippocampus, brainstem, and cerebellar GM in the naïve MS subjects after 6, 12, and 24 months of treatment initiation. This result might indicate a positive fingolimod treatment effect in MS treatment. The challenge to compare our results with literature is that the only published [ $^{11}\text{C}$ ]-PK11195 PET longitudinal study with fingolimod in MS subjects was performed only 6 months after treatment intervention. The authors (SUCKSDORFF *et al.*, 2017) showed a DVR decrease in lesions using different approach (SVCA).

In this study, SVCA approach was avoided because it is highly dependent on the PET scanner and image processing characteristics (detectors, attenuation correction, motion correction, injection time), which affects the result of reference region estimative directly.

### **6.3 STATIC PET SEMI-QUANTIFICATION**

In this study, to simplify the [ $^{11}\text{C}$ ]-PK11195 PET quantification analysis, SUVR analysis was performed using static PET images reformatted from 40-60 min after injection. NAGM and NAWB-V were evaluated as reference tissues.

For both NAGM and NAWB-V as references, SUVR is higher for MS subjects than healthy controls, which agrees with our DVR results. The results are supported by the direct relation between SUVR and DVR when the tracer concentration is at its transient-equilibrium (ITO *et al.*, 1998). In this case, we are assuming that NAGM and NAWB-V are pseudo-reference regions for [ $^{11}\text{C}$ ]-PK11195 PET quantification in MS studies.

Using NAGM as the reference tissue, SUVR does not show differences between MS subjects and healthy subjects. This result can be explained by the differences in the

NAGM DVR between MS and HC. Although, we still can show a decrease in lesions SUVR between naïve and 6 months after treatment initiation with fingolimod.

Using NAWB-V as reference tissue, SUVR shows differences between MS and healthy subjects, agreeing with our previous analysis using DVR(NAWB-V). The exclusion of brain ventricles in the reference region avoided a confounding factor due to the free tracer in this region. Regarding the longitudinal analysis, a SUVR decrease is observed for hippocampus, brainstem, and putamen between naïve and 6 months after treatment initiation, in agreement with other studies using DVR (RATCHFORD *et al.*, 2012; SUCKSDORFF *et al.*, 2017). These results reinforce the hypothesis that fingolimod treatment might be effective in MS.

Until the present moment, no studies were found evaluating the use of SUVR using NAGM and NAWB-V as references with [<sup>11</sup>C]-PK11195 PET images in MS subjects.

## 7 FINAL CONSIDERATIONS

This study aimed to investigate [ $^{11}\text{C}$ ]-PK11195 PET quantification methods for multiple sclerosis neuroinflammation.

We concluded that different MRI segmentation methods give different results for GM and WM volumes, affecting further PET quantification. The algorithm that showed the lowest variability for gray and white matter volumes segmentation was the automatic region growth algorithm implemented using the Lesion Segmentation Software (LST), which uses both T1-weighted and T2-FLAIR MR images.

The application of image-derived input function using dynamic [ $^{11}\text{C}$ ]-PK11195 PET data is still challenging due to the lack of standardization in the region of interest delineation, mainly because it is challenging to extract adjacent regions that include the uptake in the epithelial tissue. The fully quantitative with Logan Reference Model using  $t^* = 20$  min using normal-appearing whole-brain except ventricles as the reference shows the best results in the kinetic parameter DVR in order to differentiate multiple sclerosis and healthy subjects.

SUVR with the normal-appearing whole-brain except ventricles as the reference can be used with static PET images acquired from 40-60 minutes after injection. The choice of a static PET acquisition considers the difficulties to acquire and process dynamic PET data. The static PET acquisition and the use of SUVR is an excellent alternative to aid the diagnosis in clinical practice due to the compatibility of results with the dynamic PET quantification results.

Further studies are needed to investigate the optimization of image-derived input function determination, using a standardized method to segment the arteries in MRI, avoiding the inclusion of the epithelial tissue. The arteries segmentation in MRI should be validated using the input function acquired from arterial blood sampling. Moreover, another further approach is to investigate the supervised clustering analysis to determine the optimized reference region for dynamic and static [ $^{11}\text{C}$ ]-PK11195 PET images. The evaluation of parametrical maps using kinetic parameters should be another interesting topic to be performed, allowing the identification of visual differences between PET images in a voxel-based level.

## 8 REFERENCES

ALBRECHT, Daniel S. *et al.* Pseudoreference Regions for Glial Imaging with 11 C-PBR28: Investigation in 2 Clinical Cohorts. **Journal of Nuclear Medicine**, [S. l.], v. 59, n. 1, p. 107–114, 2018.

BANATI, Richard B. Visualising microglial activation in vivo. **Glia**, [S. l.], v. 40, n. 2, p. 206–17, 2002.

CHAUVEAU, Fabien *et al.* Nuclear imaging of neuroinflammation: A comprehensive review of [ 11C]PK11195 challengers. **European Journal of Nuclear Medicine and Molecular Imaging**, [S. l.], v. 35, n. 12, p. 2304–2319, 2008.

CROTEAU, Etienne *et al.* Image-derived input function in dynamic human PET/CT: methodology and validation with 11C-acetate and 18F-fluorothioheptadecanoic acid in muscle and 18F-fluorodeoxyglucose in brain. **European Journal of Nuclear Medicine and Molecular Imaging**, [S. l.], v. 37, n. 8, p. 1539–1550, 2010.

DEBRUYNE, J. C. *et al.* PET visualization of microglia in multiple sclerosis patients using [11C]PK11195. **European Journal of Neurology**, [S. l.], v. 10, n. 3, p. 257–264, 2003. Disponível em: <http://doi.wiley.com/10.1046/j.1468-1331.2003.00571.x>

DEBRUYNE, Jan C. *et al.* Semiquantification of the peripheral-type benzodiazepine ligand [11C]PK11195 in normal human brain and application in multiple sclerosis patients. **Acta neurologica Belgica**, [S. l.], v. 102, n. 3, p. 127–35, 2002. Disponível em: <http://www.ncbi.nlm.nih.gov/pubmed/12400251>

FELLHAUER, Iven *et al.* Comparison of automated brain segmentation using a brain phantom and patients with early Alzheimer's dementia or mild cognitive impairment. **Psychiatry Research: Neuroimaging**, [S. l.], v. 233, n. 3, p. 299–305, 2015. Disponível em: <http://www.ncbi.nlm.nih.gov/pubmed/26211622>. Acesso em: 25 mar. 2018.

GIANNETTI, Paolo *et al.* Microglia activation in multiple sclerosis black holes predicts outcome in progressive patients: An in vivo [(11)C](R)-PK11195-PET pilot study. **Neurobiology of Disease**, [S. l.], v. 65, p. 203–210, 2014.

HAMMERS, Alexander *et al.* Three-dimensional maximum probability atlas of the human brain, with particular reference to the temporal lobe. **Human Brain Mapping**, [S. l.], v. 19, n. 4, p. 224–247, 2003.

HAMMOUD, Dima A. *et al.* Imaging glial cell activation with [ 11 C]- R - PK11195 in patients with AIDS. **Journal of Neurovirology**, [S. l.], v. 11, n. 4, p. 346–355, 2005. Disponível em: <http://link.springer.com/10.1080/13550280500187351>

INNIS, Robert B. *et al.* Consensus nomenclature for in vivo imaging of reversibly binding radioligands. **Journal of cerebral blood flow and metabolism : official journal of the International Society of Cerebral Blood Flow and Metabolism**, [S. l.], v. 27, p. 1533–1539, 2007.

KANG, Yeona *et al.* Comparison of two different methods of image analysis for the assessment of microglial activation in patients with multiple sclerosis using ( R ) - [ N-methyl-carbon-11 ]. **PLoS ONE**, [S. l.], p. 1–14, 2018 a.

KANG, Yeona *et al.* Noninvasive PK11195-PET Image Analysis Techniques Can Detect Abnormal Cerebral Microglial Activation in Parkinson's Disease. **Journal of Neuroimaging**, [S. l.], v. 28, n. 5, p. 496–505, 2018 b.

KAUNZNER, Ulrike W. *et al.* Reduction of PK11195 uptake observed in multiple sclerosis lesions after natalizumab initiation. **Multiple Sclerosis and Related Disorders**, [S. l.], v. 15, p. 27–33, 2017. Disponível em: <https://linkinghub.elsevier.com/retrieve/pii/S2211034817300780>

KAUNZNER, Ulrike W. *et al.* Quantitative susceptibility mapping identifies

inflammation in a subset of chronic multiple sclerosis lesions. **Brain**, [S. l.], v. 142, n. 1, p. 133–145, 2019. Disponível em: <https://academic.oup.com/brain/article/142/1/133/5250435>

KOBAYASHI, Masato *et al.* 11 C-DPA-713 has much greater specific binding to translocator protein 18 kDa (TSPO) in human brain than 11 C-(R)-PK11195. **Journal of Cerebral Blood Flow & Metabolism**, [S. l.], v. 38, n. 3, p. 393–403, 2018.

KROPHOLLER, M. A. *et al.* Evaluation of reference regions for (R)-[(11)C]PK11195 studies in Alzheimer's disease and mild cognitive impairment. **J Cereb Blood Flow Metab**, [S. l.], v. 27, p. 1965–1974, 2007.

KROPHOLLER, Marc A. *et al.* Evaluation of reference tissue models for the analysis of [11C](R)-PK11195 studies. **Journal of cerebral blood flow and metabolism: official journal of the International Society of Cerebral Blood Flow and Metabolism**, [S. l.], v. 26, p. 1431–1441, 2006.

KROPHOLLER, Marc a *et al.* Development of a tracer kinetic plasma input model for (R)-[11C]PK11195 brain studies. **Journal of cerebral blood flow and metabolism: official journal of the International Society of Cerebral Blood Flow and Metabolism**, [S. l.], v. 25, n. 7, p. 842–51, 2005.

LAMMERTSMA, A. A.; HUME, S. P. Simplified reference tissue model for PET receptor studies. **NeuroImage**, [S. l.], v. 4, n. 3 Pt 1, p. 153–8, 1996.

LANGNER, Jens. **Development of a Parallel Computing Optimized Head Movement Correction Method in Positron Emission Tomography**. 2003. - Dresden University of Applied Sciences, [s. l.], 2003.

LOGAN, Jean *et al.* Graphical Analysis of Reversible Radioligand Binding from Time—Activity Measurements Applied to [N - 11 C-Methyl]-(–)-Cocaine PET Studies in Human Subjects. **Journal of Cerebral Blood Flow & Metabolism**, [S. l.], v. 10, n. 5, p. 740–747, 1990.

LOPRESTI, Brian J. *et al.* Simplified quantification of Pittsburgh Compound B amyloid imaging PET studies: a comparative analysis. **Journal of nuclear medicine: official publication, Society of Nuclear Medicine**, [S. l.], v. 46, p. 1959–1972, 2005.

LYOO, C. H. *et al.* Cerebellum Can Serve As a Pseudo-Reference Region in Alzheimer Disease to Detect Neuroinflammation Measured with PET Radioligand Binding to Translocator Protein. **Journal of Nuclear Medicine**, [S. l.], v. 56, n. 5, 2015.

PARBO, Peter *et al.* Does inflammation precede tau aggregation in early Alzheimer's disease? A PET study. **Neurobiology of Disease**, [S. l.], v. 117, p. 211–216, 2018.

PASSAMONTI, Luca *et al.* [11 C]PK11195 binding in Alzheimer disease and progressive supranuclear palsy. **Neurology**, [S. l.], v. 90, n. 22, p. e1989–e1996, 2018.

PITT, David *et al.* Imaging Cortical Lesions in Multiple Sclerosis With Ultra-High-Field Magnetic Resonance Imaging. **Archives of Neurology**, [S. l.], v. 67, n. 7, 2010.

POLITIS, Marios *et al.* Increased PK11195 PET binding in the cortex of patients with MS correlates with disability. **Neurology**, [S. l.], v. 79, n. 6, p. 523–30, 2012.

POLMAN, Chris H. *et al.* Diagnostic criteria for multiple sclerosis: 2010 revisions to the McDonald criteria. **Annals of neurology**, [S. l.], v. 69, n. 2, p. 292–302, 2011.

RATCHFORD, John N. *et al.* Decreased microglial activation in MS patients treated with glatiramer acetate. **Journal of Neurology**, [S. l.], v. 259, n. 6, p. 1199–1205, 2012. Disponível em: <http://link.springer.com/10.1007/s00415-011-6337-x>

RISSANEN, E. *et al.* In Vivo Detection of Diffuse Inflammation in Secondary Progressive Multiple Sclerosis Using PET Imaging and the Radioligand 11C-PK11195. **Journal of Nuclear Medicine**, [S. l.], v. 55, n. 6, p. 939–944, 2014. Disponível em: <http://jnm.snmjournals.org/cgi/doi/10.2967/jnumed.113.131698>

RISSANEN, Eero *et al.* Microglial activation, white matter tract damage, and disability in MS. **Neurology - Neuroimmunology Neuroinflammation**, [S. l.], v. 5, n. 3, p. e443, 2018. Disponível em: <http://nn.neurology.org/lookup/doi/10.1212/NXI.0000000000000443>

RIZZO, Gaia *et al.* Generalization of endothelial modelling of TSPO PET imaging: Considerations on tracer affinities. **Journal of Cerebral Blood Flow & Metabolism**, [S. l.], p. 0271678X1774200, 2017.

SCHMIDT, Paul *et al.* An automated tool for detection of FLAIR-hyperintense white-matter lesions in Multiple Sclerosis. **NeuroImage**, [S. l.], v. 59, n. 4, p. 3774–83, 2012. Disponível em: <http://www.ncbi.nlm.nih.gov/pubmed/22119648>. Acesso em: 27 abr. 2016.

SCHWEITZER, Pernilla J. *et al.* PET tracers for the peripheral benzodiazepine receptor and uses thereof. **Drug discovery today**, [S. l.], v. 15, n. 21–22, p. 933–42, 2010.

STOKHOLM, Morten Gersel *et al.* Assessment of neuroinflammation in patients with idiopathic rapid-eye-movement sleep behaviour disorder: a case-control study. **The Lancet Neurology**, [S. l.], v. 16, n. 10, p. 789–796, 2017.

SUCKSDORFF, Marcus *et al.* Evaluation of the Effect of Fingolimod Treatment on Microglial Activation Using Serial PET Imaging in Multiple Sclerosis. **Journal of Nuclear Medicine**, [S. l.], v. 58, n. 10, p. 1646–1651, 2017. Disponível em: <http://jnm.snmjournals.org/lookup/doi/10.2967/jnumed.116.183020>

VERSIJPT, J. *et al.* Microglial imaging with positron emission tomography and atrophy measurements with magnetic resonance imaging in multiple sclerosis: a correlative study. **Multiple Sclerosis**, [S. l.], v. 11, n. 2, p. 127–134, 2005.

YODER, Karmen K. Basic PET Data Analysis Techniques. In: MISCIAGNA, Sandro (org.). **Positron Emission Tomography - Recent Developments in Instrumentation, Research and Clinical Oncological Practice**. [S. l.]: InTech, 2013. p. 63–80.

ZANOTTI-FREGONARA, Paolo *et al.* Image-derived input function for brain PET studies: many challenges and few opportunities. **Journal of Cerebral Blood Flow & Metabolism**, [S. l.], v. 31, n. 10, 2011.



**APPENDIX A - DETAILS OF INJECTED ACTIVITY AND BODY WEIGHT FOR EACH TP.**

Group	Subject	TP1			TP2			TP3			TP4		
		Date	Weight (kg)	Inj. Activity(MBq)	Date	Weight (kg)	Inj. Activity(MBq)	Date	Weight (kg)	Inj. Activity(MBq)	Date	Weight (kg)	Inj. Activity(MBq)
Pre Treated (PT)	1	25/03/15	57	286.7	18/09/15	58	275.0	18/03/16	58	324.7	25/03/15	57	388.5
	2	27/03/15	62	373.0	5/10/2015	60	304.0	6/4/2016	64	295.0	27/03/15	62	339.1
	3	1/4/2015	56	175.4	30/09/15	61	373.9	13/04/16	58	304.6	1/4/2015	56	363.1
	4	27/03/15	65	327.4	29/09/15	65	287.1	4/4/2016	65	237.8	27/03/15	65	399.9
	5	1/4/2015	59	375.9				8/4/2016	62	275.4	1/4/2015	59	476.6
	6	18/05/15	105	404.6	16/11/15	108	407.7	6/5/2016	112	278.2	18/05/15	105	538.5
	7	25/05/15	86	383.1	23/11/15	84	333.3	1/6/2016	84	271.6	25/05/15	86	247.9
	9	19/06/15	68	364.8	16/12/15	75	279.2	15/06/16	73	297.1	19/06/15	68	301.4
	10	8/7/2015	55	374.7	20/01/16	55	321.0	20/07/16	55	305.5	8/7/2015	55	368.7
	11				17/02/16	82	338.8	2/9/2016	82	257.7	11/9/2015	65	
	12	14/09/15	58	289.5	4/3/2016	60	307.9	20/07/16	55	339.6	14/09/15	58	459.1
	Naive (N)	101	6/4/2015	59	436.6	16/10/15	58	439.7	13/04/16	60	296.8	6/4/2015	59
103		25/03/15	98	379.7	21/09/15	80	352.2				25/03/15	98	433.3
104		30/03/15	47	318.6	2/10/2015	47	334.2				30/03/15	47	456.3
105		15/05/15	67	414.1				11/5/2016	68	280.7	15/05/15	67	433.8
106		22/05/15	53	412.2	25/11/15	56	325.9	10/6/2016	56	279.3	22/05/15	53	403.1
107		29/05/15	83	363.2	27/11/15	85	329.4	13/05/16	85	294.5	29/05/15	83	458.8
108		12/6/2015	77	362.0	14/12/15	74	357.5	10/6/2016	76	326.8	12/6/2015	77	458.6
109		6/7/2015	64	284.2	20/01/16	64	310.9	17/08/16	64	313.8	6/7/2015	64	523.8
110		31/08/15	51	301.9	2/3/2016	53	354.2	19/08/16	53	374.4	31/08/15	51	281.1
111		2/9/2015	67	303.5	15/02/16	66	295.7	19/08/16	66	316.9	2/9/2015	67	358.7
112		23/09/15	53	351.5	11/3/2016	53	360.6	21/09/16	53	338.5	23/09/15	53	342.9
Healthy Controls (HC)		501	17/07/15	89	345.6	-	-	-	-	-	-	-	-
	502	1/7/2015	65	390.5	-	-	-	-	-	-	-	-	-
	505	21/10/15	78	506.2	-	-	-	-	-	-	-	-	-
	506	28/10/15	67	262.0	-	-	-	-	-	-	-	-	-
	507	4/11/2015	72	304.3	-	-	-	-	-	-	-	-	-
	509	11/5/2016	62	293.4	-	-	-	-	-	-	-	-	-
	510	22/07/16	88	479.2	-	-	-	-	-	-	-	-	-
	511	17/08/16	65	299.2	-	-	-	-	-	-	-	-	-
	512	31/08/16	60	342.7	-	-	-	-	-	-	-	-	-
	513	9/12/2016	78	311.3	-	-	-	-	-	-	-	-	-

**APPENDIX B – PAPER “COMPARAÇÃO DA SEGMENTAÇÃO AUTOMATIZADA DE IMAGENS DE MRI CEREBRAIS EM PACIENTES COM ESCLEROSE MÚLTIPLA E SUJEITOS SAUDÁVEIS” PRESENTED AT THE XXIII BRAZILIAN CONGRESS OF MEDICAL PHYSICS, PORTO ALEGRE, 2018.**

**Comparação da segmentação automatizada de imagens de MRI cerebrais em pacientes com esclerose múltipla e sujeitos saudáveis**  
Comparison of automated brain MRI segmentation in patients with multiple sclerosis and healthy subjects

Phelipi N. Schuck<sup>1</sup>, Caroline M. Dartora<sup>1</sup>, Marcelo M. Delucis<sup>1</sup>, Aline Kotoski<sup>2</sup>, Giordani R. dos Passos<sup>3</sup>, Vincenzo A. Sangalli<sup>4</sup>, Márcio S. Pinho<sup>3,4</sup>, Alexandre R. Franco<sup>2,3</sup>, Michele A. Andrade<sup>1</sup>, Ana M. Marques da Silva<sup>1,3</sup>, Jefferson Becker<sup>3</sup>

<sup>1</sup>PUCRS, Núcleo de Pesquisa em Imagens Médicas, Porto Alegre/RS, Brasil

<sup>2</sup>PUCRS, Laboratório de Imagens, Porto Alegre/RS, Brasil

<sup>3</sup> PUCRS, Instituto do Cérebro do Rio Grande do Sul, Porto Alegre/RS, Brasil

<sup>4</sup> Grupo de Realidade Virtual, Porto Alegre/RS, Brasil

---

**Resumo**

Imagens de alta resolução estrutural, como o imageamento por ressonância magnética, permitem a investigação de doenças neurodegenerativas, como a esclerose múltipla. Alterações morfológicas e estruturais podem ser analisadas através da segmentação de regiões em imagens por ressonância magnética. Atualmente, softwares de segmentação automática são utilizados para agilizar o processo de análise das imagens. O objetivo deste trabalho é comparar a volumetria da substância branca e da substância cinzenta, obtidas a partir das segmentações de imagens por ressonância magnética cerebral, realizadas com o uso dos softwares SPM8, LST, Freesurfer e SienaX, em 24 pacientes com esclerose múltipla e 11 sujeitos controles. Os softwares que melhor diferenciam os grupos de controles e pacientes são os softwares SPM8, LST e SienaX sem normalização espacial. Percebe-se que, quando as imagens são normalizadas espacialmente pelo software SienaX, ocorre uma superestimação dos volumes de substância branca, substância cinzenta e cérebro total. Mais estudos são necessários para comparar as segmentações com padrões-ouro, como *phantoms* e delimitação manual feitas por médicos radiologistas.

**Palavras-chave:** MRI; Segmentação; Volumetria; Esclerose Múltipla.

**Abstract**

*High resolution structural images, such as Magnetic Resonance Imaging allow neurodegenerative diseases investigation i.e. multiple sclerosis. Morphologic and structural mutation can be analyzed through MRI segmentation. Currently, automated segmentation software is used to streamline the image analysis process. The aim of this study is to compare volume measures from white matter, gray matter from brain MRI segmented images done by softwares SPM8, LST, Freesurfer and SienaX with 24 multiple sclerosis patients and 11 healthy controls. The softwares that best differentiate the control groups and patients are the software SPM8, LST and SienaX without spatial normalization. When the images are spatially normalized by the software SienaX, there is an overestimation of the volumes of white matter, gray matter and whole brain. More studies are needed to compare segmentations with gold standards such as phantoms and manual delimitation by medical radiologists.*

**Keywords:** MRI; Segmentation; Volume measure; Multiple Sclerosis.

---

**1. Introdução**

Imagens de alta resolução estrutural, como o imageamento por ressonância magnética ou MRI (*Magnetic Resonance Imaging*) permitem a investigação de doenças neurodegenerativas, como a esclerose múltipla ou MS (*Multiple Sclerosis*)<sup>1</sup>. A MS pode causar alterações estruturais e morfológicas, tanto na substância branca, quanto em substância cinzenta, podendo ser acompanhadas por estudos baseados em MRI<sup>2</sup>.

Na MRI cerebral são obtidas imagens de alta resolução espacial do cérebro, o que leva a um grande volume de dados a serem processados<sup>3</sup>. Com o crescente uso de técnicas de aquisição de imagens médicas, é necessária a utilização de *softwares* para o processamento (realinhamento, correção, segmentação, suavização, correção de

ruído e não homogeneidade de campo) e a análise dessas imagens<sup>4,5</sup>.

Os métodos de segmentação de imagens utilizam algoritmos que delimitam regiões de interesse, como estruturas ou regiões anatomicamente bem definidas. Além da segmentação manual, podem ser implementados métodos de segmentação semiautomática e automática. Com o avanço da tecnologia, automatizar o processo de segmentação de imagens tem se tornado cada vez mais importante para aprimorar a visualização anatômica e funcional do cérebro<sup>6</sup>.

A segmentação de MRI cerebral divide a imagem em um conjunto de regiões homogêneas não sobrepostas, que possuem atributos semelhantes, tais como a intensidade do pixel e textura<sup>7</sup>. No caso da MRI cerebral, as principais estruturas são

classificadas em três grandes tipos: substância branca (WM, *white matter*), substância cinzenta (GM, *gray matter*) e líquido cefalorraquidiano (CSF, *cerebrospinal fluid*). Os resultados da segmentação são posteriormente utilizados em diversas aplicações, tais como análise de estruturas anatômicas, estudo de regiões patológicas ou planejamento cirúrgico <sup>7</sup>.

Apesar dos avanços no desenvolvimento de algoritmos para segmentação em MRI cerebral, ainda existem dificuldades que geram resultados distintos produzidos por diferentes técnicas, para a mesma imagem. Essas se devem ao ruído, proveniente do equipamento em si e sua eletrônica; à não uniformidade do campo de excitação de radiofrequência, que gera pequenas variações de intensidade de pixel dentro de tecidos homogêneos; e ao efeito de volume parcial, quando o sinal de um voxel contribui para múltiplos voxels adjacentes <sup>6</sup>.

Na maioria dos casos de imagens 3D, a segmentação é realizada em um conjunto de imagens 2D, corte a corte, onde é necessário um pós-processamento para realizar a junção dos cortes para formar o volume. A grande diferença entre as segmentações 2D e 3D está nos elementos de processamento, pixels e voxels, em que as imagens são calculadas. Na prática, técnicas de segmentação de imagens 2D podem ser utilizadas para o espaço 3D, porém com o custo de ser necessário um maior poder de processamento da máquina e perda de informações devido à mudança de espaço, sendo este último fator relevante ao ser realizado volumetria de estruturas.<sup>3</sup>

O objetivo deste trabalho é comparar a volumetria da WM e da GM obtidas a partir de segmentações de MRI cerebral feitas através de quatro software: *Statistical Parametric Mapping 8* (SPM8), *Lesion Segmentation Toolbox* (LST), *Freesurfer* e *SienaX*, em pacientes com MS e sujeitos controles.

## 2. Materiais e Métodos

### 2.1 Dados do Estudo

As imagens de MRI utilizadas neste estudo referem-se a exames realizados em indivíduos voluntários do projeto “Avaliação da ativação microglial pelo PET/CT e associação com o aparecimento de lesões na Ressonância Magnética em pacientes com Esclerose Múltipla remitente-recorrente submetidos a tratamento com fingolimode” (CAAE 23949813.7.0000.5336, parecer 1.094.228). Foram utilizadas imagens de 24 pacientes com esclerose múltipla [(31 ± 7) anos, mínimo 20 anos e máximo 48 anos, e (71 ± 9) kg] e 11 imagens de indivíduos saudáveis [(31 ± 7) anos, mínimo 20 anos e máximo 48 anos, e (71 ± 9) kg].

### 2.2 Aquisição das imagens

As MRI foram adquiridas em um equipamento de ressonância magnética GE Healthcare Signa HDxt de 3,0 T. Foram adquiridas imagens de MR estruturais de alta resolução ponderadas em T1, utilizando sequência BRAVO™, da GE Healthcare, com tempo de repetição de 2400 ms; tempo de eco de 16 ms;

campo de visão de 220 mm; com voxels isotrópicos de 1 mm. As imagens ponderadas em T1 apresentam matriz de 512 x 512 x 196 pixels (240,03 x 240,03 x 196,00 mm<sup>3</sup>), 16-bits por pixel, resolução de 2,133 pixels/mm, tamanho de voxel de 0,47 x 0,47 x 1,00 mm<sup>3</sup>, e intervalo de quadros de 6,12 ms. Foram adquiridas imagens ponderadas em T2, utilizando a sequência FLAIR 3D, com tempo de repetição de 6000 ms; tempo de eco de 125 ms; campo de visão de 220 mm; com voxel isotrópico de 1 mm. As imagens ponderadas em T2 apresentam matriz de 512 x 512 x 180 pixels (256 x 256 x 180 mm<sup>3</sup>), 32-bits por pixel, resolução de 2 pixel/mm e tamanho de voxel 0,5x 0,5 x 1,0 mm<sup>3</sup>.

### 2.3 Processamento das imagens

As imagens foram processadas com os softwares SPM 8, LST, Freesurfer e SienaX. O processamento das imagens foi realizado através de técnicas padrões de realinhamento e correção, seguidos de segmentação, normalização, suavização e análise, presentes em cada software. A qualidade das imagens e qualidade das segmentações foram inspecionadas visualmente. As subseções a seguir apresentam os detalhes do processamento em cada *software*.

#### 2.3.1 SPM8

O SPM8 é um aplicativo utilizado no Matlab R2012b (<http://www.fil.ion.ucl.ac.uk/spm/>), desenvolvido para diversas modalidades de imagem cerebral, tanto funcionais e metabólicas quanto anatômicas (fMRI, MRI, PET/CT, SPECT, EEG e MEG). Para a segmentação de WM, GM e CSF, o software utiliza de mapas paramétricos de probabilidade de tecidos do ICBM (*International Consortium for Brain Mapping*), baseado em MRI ponderadas em T1 de 452 sujeitos no espaço MNI (*Montreal Neurological Institute*). Foram utilizados os seguintes parâmetros no processamento: filtro de suavização de 4mm de frequência espacial e regularização de *bias* leve (0,001), padrões do software.

#### 2.3.2 LST

O LST é uma ferramenta implementada no SPM8 que utiliza correção, normalização, retirada de caixa craniana, suavização e análise do SPM8 <sup>8</sup>. No entanto, sua implementação utiliza algoritmo de crescimento de região para a segmentação dos tecidos de interesse. Para esse algoritmo são utilizadas MRI ponderadas em T1 e em T2-FLAIR, registradas e normalizadas espacialmente entre si, onde ocorre a estimativa de valor de pixel entre as duas sequências de MRI, gerando um mapa de probabilidade de região, onde constam a WM, GM e CSF. Foram utilizados os seguintes parâmetros no processamento: filtro de suavização de 4mm de frequência espacial e regularização de *bias* leve (0,001), padrões do software.

### 2.3.3 FreeSurfer

A implementação do software Freesurfer utiliza um atlas que, ao ser normalizado com a imagem de entrada, atribui valores de classificação para WM, GM e CSF<sup>9</sup>. O atlas baseia-se em informações probabilísticas do posicionamento das estruturas. A estatística atribuída a cada tecido (médias e matrizes de covariância) são tabeladas regionalmente ao longo do espaço do atlas, usando um algoritmo linear otimizado para registrar cada cérebro com um valor médio. As probabilidades são computadas via histograma de frequências no espaço do atlas, permitindo o cálculo de probabilidade de que uma classe anatômica ocorra em uma área específica do atlas. Por fim, a probabilidade resultante de um determinado arranjo espacial é incorporada no procedimento final da segmentação. Cada probabilidade é calculada a partir de um conjunto de treinamento para cada ponto no atlas, modelando a segmentação como um campo aleatório anisotrópico não-estacionário de Markov.

### 2.3.4 SienaX

O SienaX, implementado no software FSL<sup>10,11</sup> estima o volume cerebral a partir de uma única imagem.<sup>12,13</sup> O primeiro processo do SienaX é realizar a separação entre o tecido cerebral e o crânio. O método é conhecido como BET (do inglês, *Brain Extraction Tool*), que utiliza um modelo que se ajusta com a superfície cerebral, permitindo deformações de acordo com as regiões cerebrais. As imagens são normalizadas em relação ao atlas padrão MNI152<sup>14-16</sup>. No processo de segmentação, o modelo utilizado é o HMRF (do inglês, *Hidden Markov Random Field*) e o algoritmo utilizado é o de maximização de expectativa (do inglês, *Expectation-Maximization Algorithm*). A imagem é então segmentada em WM, GM, CSF e *background*,

gerando a estimativa do volume total cerebral. A segmentação do SienaX inclui estimativa de volumes parciais para todos os voxels do volume cerebral e não somente para os voxels da superfície cerebral. A segmentação pode ser realizada tanto no espaço original da MRI (SienaX\_UN), quanto no espaço normalizado pelo tamanho da cabeça do sujeito (SienaX\_NORM).

### 2.4 Análise dos dados

Os resultados foram analisados por meio do teste ANOVA, com valor de significância  $p \leq 0,05$ , com um grau de liberdade ( $df = 1$ ).

Para analisar a correlação entre os dados obtidos foi utilizado o coeficiente de correlação intraclassa (ICC), com modelo aleatório de dois fatores do tipo consistência.

Para analisar a diferença entre os softwares foi utilizado o teste *t* de Student pareado, com valor de significância  $p \leq 0,05$ .

Todos os testes estatísticos foram realizados com o software IBM SPSS Statistics 23.0.

## 3. Resultados

A tabela 1 apresenta os resultados obtidos a partir da volumetria das regiões de WM, GM e todo cérebro (WB, *whole brain*) para cada um dos softwares e para os grupos Pacientes e Controles do estudo.

Para fins de melhor visualização dos dados e comparação visual dos resultados, foram feitos gráficos do tipo caixa (*box-plot*), apresentados nas Figuras 1, 2 e 3.

As tabelas 2, 3 e 4 mostram as diferenças estatísticas entre os softwares analisados, comparando região por região, de forma pareada, através do teste *t* de Student. O valor de significância é  $p \leq 0,05$ .

Tabela 1. Volumes calculados de WM, GM e WB, utilizando os softwares Freesurfer, LST, SienaX não normalizado, SienaX normalizado e SPM8.

Softwares	Todos N = 37	Pacientes (N = 24)	Controles (N = 11)	ANOVA		
				F	df	p
WM Freesurfer	476,84 ± 50,68	465,50 ± 45,25	499,53 ± 55,11	3,238	1	0,083
WM LST	518,49 ± 69,18	495,84 ± 62,17	578,88 ± 48,89	12,952	1	0,001'
WM SienaX Não Norm	538,91 ± 71,21	518,98 ± 65,44	582,39 ± 66,01	7,045	1	0,012'
WM SienaX Norm	727,46 ± 58,90	716,75 ± 61,10	750,85 ± 48,32	2,65	1	0,113
WM SPM8	449,41 ± 56,27	432,78 ± 47,13	485,71 ± 59,52	8,062	1	0,008'
GM Freesurfer	644,60 ± 53,83	639,41 ± 50,23	655,50 ± 62,10	0,597	1	0,446
GM LST	647,46 ± 64,28	630,93 ± 58,55	691,53 ± 60,58	6,887	1	0,013'
GM SienaX Não Norm	605,64 ± 59,15	594,66 ± 52,70	629,58 ± 67,74	2,765	1	0,106
GM SienaX Norm	815,17 ± 42,18	816,95 ± 44,87	811,45 ± 27,67	0,123	1	0,728
GM SPM8	712,40 ± 80,75	694,08 ± 72,59	752,37 ± 86,52	4,314	1	0,046'
WB Freesurfer	1115,31 ± 106,28	1096,39 ± 101,11	1155,02 ± 111,10	2,14	1	0,154
WB LST	1165,95 ± 120,62	1126,78 ± 105,32	1270,41 ± 97,08	12,665	1	0,001'
WB SienaX Não Norm	1144,54 ± 121,27	1113,64 ± 107,04	1211,97 ± 127,90	5,635	1	0,024'
WB SienaX Norm	1546,99 ± 82,24	1539,98 ± 87,59	1562,30 ± 70,50	0,548	1	0,464
WB SPM8	1161,81 ± 129,90	1126,85 ± 110,78	1238,08 ± 140,77	6,41	1	0,016'

\*Diferença estatisticamente significativa.

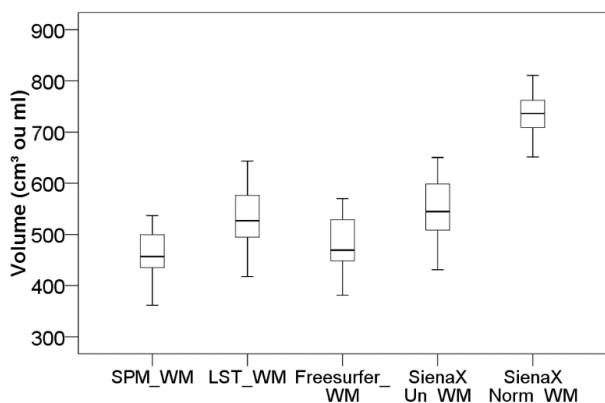


Figura 1. Gráfico do tipo caixa mostrando o volume segmentado na região da WM

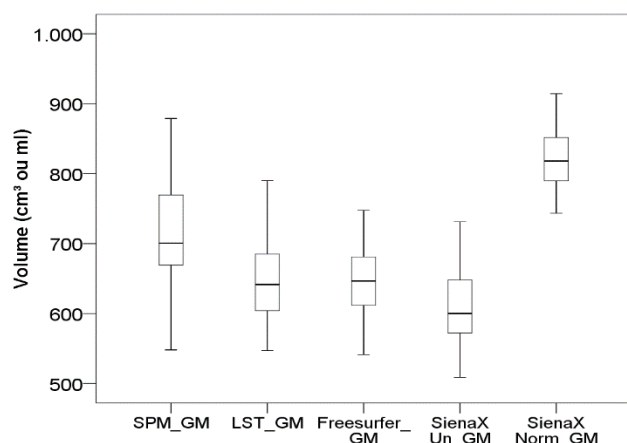


Figura 2. Gráfico do tipo caixa mostrando o volume segmentado na região da GM.

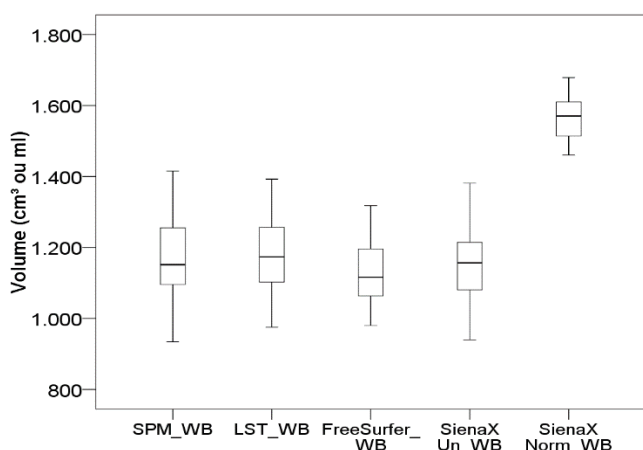


Figura 3. Gráfico do tipo caixa mostrando o volume segmentado de WB.

Tabela 2. Resultados da análise estatística utilizando teste *t* de Student para os volumes de WM

Softwares	t value	p value
SPM x LST	-4,529	0,234
SPM x FreeSurfer	-2,050	0,720
SPM x SienaX	-5,833	0,211
SPM x SienaX Norm	-20,193	0,835
LST x FreeSurfer	2,703	0,129
LST x SienaX Un	-1,198	0,936
LST x SienaX Norm	-13,437	0,199
FreeSurfer x SienaX	-3,985	0,119
FreeSurfer x SienaX Norm	-18,225	0,915
SienaX Un x SienaX Norm	-12,070	0,179

Tabela 3. Resultados da análise estatística utilizando teste *t* de Student para os volumes de GM

Softwares	t value	p value
SPM x LST	3,655	0,289
SPM x FreeSurfer	3,959	0,038
SPM x SienaX Un	6,310	0,094
SPM x SienaX Norm	-6,597	0,002
LST x FreeSurfer	0,192	0,213
LST x SienaX Un	2,794	0,476
LST x SienaX Norm	-12,663	0,010
FreeSurfer x SienaX Un	2,785	0,589
FreeSurfer x SienaX Norm	-14,286	0,210
SienaX Un x SienaX Norm	-16,898	0,070

Tabela 4. Resultados da análise estatística utilizando teste *t* de Student para os volumes de WB

Softwares	t value	p value
SPM x LST	-0,136	0,701
SPM x FreeSurfer	1,579	0,251
SPM x SienaX Un	0,575	0,652
SPM x SienaX Norm	-14,822	0,010
LST x FreeSurfer	1,778	0,428
LST x SienaX Un	0,729	0,943
LST x SienaX Norm	-15,298	0,022
FreeSurfer x SienaX Un	-1,035	0,477
FreeSurfer x SienaX Norm	-18,566	0,136
SienaX Un x SienaX Norm	-16,249	0,030

Tabela 5. Resultados da análise de coeficiente de correlação interclasse (ICC) entre todos os softwares.

Volume Segmentado	ICC
WM	0,755
GM	0,644
WB	0,646

#### 4. Discussão

A segmentação de quatro sujeitos provenientes do software FreeSurfer foram excluídas, por não passarem pela inspeção de qualidade, os demais softwares realizaram segmentações de forma satisfatória.

Foi possível verificar na tabela 1 que a WM e segmentada pelos softwares LST, SienaX sem normalização e SPM8 possibilitam a diferenciação estatística entre os grupos de pacientes e controles. Diferenciam-se de forma estatisticamente significativa os grupos de controle e pacientes quando comparadas suas áreas de GM segmentadas pelos softwares SPM8 e LST. Quando comparados os volumes de WB, os softwares que possibilitam a diferenciação entre os grupos são LST, SienaX sem normalização e SPM8

Quando comparados os volumes segmentados de todos os sujeitos se percebe que o software SienaX se diferencia de forma significativamente dos demais, tanto na análise visual dos gráficos de caixa (Figuras 1, 2 e 3), quanto na análise estatística através do teste *t* (Tabelas 2, 3 e 4).

Além disso, foram calculados os coeficientes de correlação interclasse (ICC) entre os grupos. A correlação entre os dados varia de forte para a WM e moderada para GM e WB, quando comparados todos softwares. Quando retirados os volumes de segmentação feitos pelo software SienaX com as imagens normalizadas espacialmente, os ICCs apresentam correlação forte entre os demais

softwares ( $ICC^{WM} = 0,857$ ;  $ICC^{GM} = 0,857$  e;  $ICC^{WB} = 0,864$ ).

Os resultados do presente estudo corroboram com o estudo de Fellhauer e colaboradores (2015), onde são comparados pacientes com doença de Alzheimer, declínio cognitivo leve e grupos controles. Não se observaram diferenças significativas quando comparados os volumes entre os softwares SPM8, *SienaX* e *FreeSurfer* sem imagens normalizadas espacialmente.

No estudo de Fellhauer e colaboradores (2015) verificaram-se diferenças entre os volumes de WM em grupos de pacientes e controle utilizando o softwares *SienaX* e *FreeSurfer* e diferenças em GM através dos softwares SPM8, *SienaX* e *FreeSurfer*.

## 5. Conclusões

Este estudo apresenta uma avaliação ampla dos volumes segmentados de WM, GM e WB usando quatro diferentes softwares. Conclui-se que não há diferença estatisticamente significativa entre os volumes segmentados, exceto quando é feita a normalização espacial utilizando o software *SienaX*, devido à superestimação dos volumes de WM, GM e WB. Além disso, pode-se concluir que os softwares SPM8, LST e *SienaX* diferenciam melhor os grupos de controles e pacientes. Mais estudos são necessários para comparar as segmentações com padrões ouro, como *phantoms* e delimitação manual feitas por médicos radiologistas.

## Agradecimentos

O presente trabalho foi realizado com apoio da Coordenação de Aperfeiçoamento de Pessoal Nível Superior – Brasil (CAPES) – Código de Financiamento 001”. Este estudo foi apoiado financeiramente pela Novartis. Os autores não recebem qualquer reembolso ou benefícios financeiros e declaram que não têm interesses conflitantes. Novartis não desempenhou qualquer papel na concepção, métodos, gestão de dados ou análise ou na decisão de publicar.

## Referências

1. van Walderveen, M. A. *et al.* Histopathologic correlate of hypointense lesions on T1-weighted spin-echo MRI in multiple sclerosis. *Neurology* **50**, 1282–8 (1998).
2. Wegner, C., Esiri, M. M., Chance, S. A., Palace, J. & Matthews, P. M. Neocortical neuronal, synaptic, and glial loss in multiple sclerosis. *Neurology* **67**, 960–7 (2006).
3. Despotović, I., Goossens, B. & Philips, W. MRI Segmentation of the Human Brain: Challenges, Methods, and Applications. *Comput. Math. Methods Med.* **2015**, 1–23 (2015).
4. Fellhauer, I. *et al.* Comparison of automated brain segmentation using a brain phantom and patients with early Alzheimer's dementia or mild cognitive impairment. *Psychiatry Res. Neuroimaging* **233**, 299–305 (2015).
5. Pham, D. L., Xu, C. & Prince, J. L. Current Methods in Medical Image Segmentation. *Annu. Rev. Biomed. Eng.* **2**, 315–337 (2000).
6. Eford, N. *Digital image processing : a practical introduction using Java.* (Addison-Wesley, 2000).
7. Balafar, M. A., Ramli, A. R., Saripan, M. I. & Mashohor, S. Review of brain MRI image segmentation methods. *Artif. Intell. Rev.* **33**, 261–274 (2010).
8. Schmidt, P. *et al.* An automated tool for detection of FLAIR-hyperintense white-matter lesions in Multiple Sclerosis. *Neuroimage* **59**, 3774–83 (2012).

9. Fischl, B. *et al.* Whole brain segmentation: automated labeling of neuroanatomical structures in the human brain. *Neuron* **33**, 341–55 (2002).
10. Smith, S. M. *et al.* Advances in functional and structural MR image analysis and implementation as FSL. *Neuroimage* **23**, S208–S219 (2004).
11. Jenkinson, M., Beckmann, C. F., Behrens, T. E. J., Woolrich, M. W. & Smith, S. M. Fsl. *Neuroimage* **62**, 782–790 (2012).
12. Smith, S. M., De Stefano, N., Jenkinson, M. & Matthews, P. M. Normalized accurate measurement of longitudinal brain change. *J. Comput. Assist. Tomogr.* **25**, 466–75 (2001).
13. Smith, S. M. *et al.* Accurate, Robust, and Automated Longitudinal and Cross-Sectional Brain Change Analysis. *Neuroimage* **17**, 479–489 (2002).
14. Jenkinson, M. & Smith, S. A global optimisation method for robust affine registration of brain images. *Med. Image Anal.* **5**, 143–56 (2001).
15. Smith, S. M. Fast robust automated brain extraction. *Hum. Brain Mapp.* **17**, 143–155 (2002).
16. Jenkinson, M., Bannister, P., Brady, M. & Smith, S. Improved optimization for the robust and accurate linear registration and motion correction of brain images. *Neuroimage* **17**, 825–41 (2002).



Pontifícia Universidade Católica do Rio Grande do Sul  
Pró-Reitoria de Graduação  
Av. Ipiranga, 6681 - Prédio 1 - 3º. andar  
Porto Alegre - RS - Brasil  
Fone: (51) 3320-3500 - Fax: (51) 3339-1564  
E-mail: [prograd@pucrs.br](mailto:prograd@pucrs.br)  
Site: [www.pucrs.br](http://www.pucrs.br)